Journal of Fluids and Structures 115 (2022) 103785

Contents lists available at ScienceDirect

Journal of Fluids and Structures

journal homepage: www.elsevier.com/locate/jfs

Hydrodynamic interactions between waves and cylinder arrays of relative motions composed of truncated floating cylinders with five degrees of freedom

Xiaohui Zeng [a,b,c], Qi Wang [a,b], Min Shi [a,b], Yuanshun Kang [a,b], Fajun Yu [d,e,*]

[a] Institute of Mechanics, Chinese Academy of Sciences, Beijing 100190, China
[b] School of Engineering Science, University of Chinese Academy of Sciences, Beijing 100049, China
[c] State Key Laboratory of Coastal and Offshore Engineering, Dalian University of Technology, Dalian 116024, China
[d] Qingdao Innovation and Development Base, Harbin Engineering University, Qingdao 266000, China
[e] College of Shipbuilding Engineering, Harbin Engineering University, Harbin 150001, China

ARTICLE INFO

Article history:
Received 3 May 2022
Received in revised form 7 October 2022
Accepted 22 October 2022
Available online 14 November 2022

Keywords:
Wave-structure interaction
Relative motion
Semi-analytical method
Radiation–diffraction
Wave energy converter array

ABSTRACT

The hydrodynamic interactions between waves and a truncated floating circular cylinder array were examined in this work. Each cylinder of the array is allowed to oscillate with five degrees of freedom (DOFs), and there can be relative motions among different cylinders. The hydrodynamic responses of such arrays in the presence of ambient incident waves were studied using a semi-analytical technique, in which, the unknown coefficients of radiation–diffraction velocity potentials caused by array motions were expressed by the linear combination of each cylinder's to-be-calculated oscillation amplitudes in each direction. Then, for each cylinder in the array, the amplitude of each degree of freedom was computed. Variations in the oscillation amplitudes of the cylinders in the array with wavenumbers for various incidence angles and column spacing, and amplitude distributions of free surface elevation for various wavenumbers were given. Additionally, extensions to the situation of multidirectional irregular waves were presented. Last but not least, we examined the effects of other DOFs (nonheave) on hydrodynamic responses and wave energy extraction performances (capture width w and interaction factor q) by comparing the results obtained by the 5-DOF and the 1-DOF (heave) models. In terms of response amplitude and wave energy extraction performance, the 5-DOF model's results were significantly different from those of the 1-DOF model. Therefore, it is suggested to use the 5-DOF model to analyze such cylindrical arrays.

1. Introduction

Since many floating offshore engineering structures may be described as cylinder arrays, the interaction between cylinders and waves is a key topic in the hydrodynamics of ocean engineering. When the hydrodynamic analysis of the interaction between cylinder arrays and waves is conducted, these arrays can be roughly divided into two categories. The floating bodies of offshore drilling and production platforms (such as semi-submersibles and tension leg platforms) and the floating foundations of offshore wind turbines can be classified into one category. These floating bodies can be

* Corresponding author at: Qingdao Innovation and Development Base, Harbin Engineering University, Qingdao 266000, China.
E-mail address: yufajun@hrbeu.edu.cn (F. Yu).

https://doi.org/10.1016/j.jfluidstructs.2022.103785
0889-9746/

thought of as such a cylinder array, in which the cylinders are rigidly connected to each other. The array's cylinders move collectively because there is no relative motion between them. However, in the other category of arrays, such as an oscillating buoy type wave energy converter array, there are relative motions among cylinders and the array does not move as a whole. The hydrodynamic issue with such arrays has gained more and more attention recently and is also the focus of this work.

The hydrodynamic problems of complex-shaped floating bodies are usually solved by numerical methods such as the boundary element method/ finite element methods, or a combination of numerical and analytical methods. While for the floating bodies with regular cross sections (such as circle, ellipse and some smoothly shapes), it can be solved by analytical method. Over the years, a variety of analytical and semi-analytical methods have been proposed to analyze the above hydrodynamic problems of cylinder arrays. Okhusu (1974) used the iterative multiple scattering method to analyze the diffraction problem of a group of vertical cylinders. Mavrakos and Koumoutsakos (1987) extended this method to axisymmetric objects of arbitrary shape. Konispoliatis and Mavrakos (2016) used this method to investigate the bottomless oscillation water column array. Spring and Monkmeyer (1975) applied the direct matrix method to the diffraction problem of bottom-mounted cylinders, in this method component waves of each cylinder are obtained at the same time without iteration. Linton and Evans (1990) developed this method and derived a simplified form of velocity potential. Kagemoto and Yue (1986) derived an exact algebraic method to solve the diffraction and radiation problem of an array of bodies in waves, and the solution and characteristics of the diffraction transfer matrix have been further studied by Mcnatt et al. (2015), Flavia and Meylan (2019). Mavrakos et al. (2018) compared the results obtained by the multiple scattering method and direct method for wave diffraction on truncated cylinders, and found that they are in good agreement. In addition, there are some approximation methods. For the case of large spacing between cylinders, the plane-wave approximation method (Simon, 1982; Williams and Abul-Azm, 1989; Singh and Babarit, 2014) can be used. For the case that the wavelength and cylinder spacing are much larger than the characteristic size of the cylinder, the point absorber approximation (Falnes, 1980; Thomas and Evans, 1981; McGuinness and Thomas, 2016) can be adopted. For a great number of bodies, Kashiwagi (2017) developed a hierarchical method to analyze the hydrodynamic interactions.

For water wave diffraction by an array of fixed cylinders, from Okhusu (1974) and Spring and Monkmeyer (1975) to Linton and Evans (1990), people have obtained the solution of this problem. In recent years, phenomena such as trapping and near-trapping in the water wave diffraction of some specific geometric cylinder arrays have also been observed (e.g., a large number of circular cylinders arranged in a row, cylinders arranged along a circle, arrays containing cylinder position perturbation, etc.). Studies on these phenomena have greatly deepened the understanding of the diffraction problem of cylinder arrays. Maniar and Newman (1997) found that the wave forces on a long array of bottomed cylinders could increase significantly at certain wavenumbers. Evans and Porter (1997) and Chatjigeorgiou et al. (2019) investigated similar cases in the wave diffraction of a circular array of bottomed cylinders and a long array of truncated cylinders. Zeng et al. (2019) studied the regular fluctuation phenomenon of wave forces in non-trapped regions of a long array of bottomed cylinders and proposed prediction formulas. Bennetts et al. (2017) studied the influence of cylinder position changes on the maximum peak load of the original array in a long array of cylinders. Chatjigeorgiou (2019) investigated wave diffraction by an array of truncated cylinders in front of a vertical wall. For cylinder arrays that can oscillate in waves, in addition to obtaining the wave excitation forces by solving the wave diffraction problem, it is also necessary to study the radiated waves generated by the oscillations of the cylinders. Based on the method of Kagemoto and Yue (1986), Yilmaz (1998) studied the radiation problem of truncated-cylinder array moving as a whole, and gave the hydrodynamic coefficients. Siddorn and Taylor (2008) studied the radiation problem of cylinder array with relative motions and gave the concrete results in the case of cylinders making translational oscillations. Zeng and Tang (2013) and Zeng et al. (2016) gave concrete results on the radiation problem of such an array with both translation and rotation oscillations.

After studying the wave diffraction and radiation of cylinder arrays, combined with the structural dynamics equation, dynamic responses, such as displacements of the floating cylinder array in the presence of incident waves can also be solved. At this time, however, the motion of the cylinder array is unknown before solving, which is different from the radiation problem of prescribed motion in advance. For those cylinder arrays that can be regarded as a whole (e.g., floating bodies of semi-submersibles/tension leg platforms), there has been a lot of work on its response in the presence of incident waves for many years. For this type of cylinder array, the recent work is more on the response mitigation and optimal design (Odijie et al., 2017; Zhang et al., 2018, 2020). In recent years, wave energy extraction has received renewed attention from industries and academia. The wave energy converter (WEC) array composed of multiple floating bodies is a typical offshore wave power farm type. Many studies investigated the influences of buoy size and spacing, buoy number, array layout, wave climate, and power take-off control strategy on the performance of these WEC arrays (Child and Venugopal, 2010; Göteman, 2017; Penalba et al., 2017; Sharp and DuPont, 2018; Balitsky et al., 2018; Tokić and Yue, 2019; Zhong and Yeung, 2019; Giassi et al., 2020). There is no structural connection among the floating buoys in a WEC array, and there are relative motions among the buoys under the action of waves. Therefore, this type of array could not be regarded as a whole, making it necessary to analyze the different motions of each cylinder. Each cylinder in such an array has multi-degree-of-freedom (DOF) (i.e. translations and rotations in various directions). However, most existing studies have only considered the heave motion of each cylinder in the analysis. In these works, the 1-DOF heave model of each cylinder was used to analyze the array's hydrodynamic characteristics and motion responses. At present, few concrete analysis results have been published on the motion responses of an independently oscillating cylinder array in which each cylinder has multi-DOF. Whether the WEC array analysis based on a single DOF model can accurately reflect the

situation of multi-DOF remains to be further studied. This study shows that the results considering multi-DOF motions of each cylinder are significantly different from that of the single DOF (as shown in Section 4 of this paper). It is necessary to study the motion responses of an array with multi-DOF in the presence of ambient incident waves. This investigation might not only help to establish a more reasonable hydrodynamic analysis model but also help to improve the design of oscillating buoy type WEC array to improve the energy extraction efficiency, structural safety, and service life.

In this paper, the diffraction, radiation, and motion responses of truncated cylinders in an independently oscillating cylinder array in the presence of incident waves were studied by a semi-analytical method. The amplitude of each cylinder's DOF in the array, the amplitude distributions of free surface elevation around the array, and the wave energy extraction performance (capture width w and interaction factor q) were given. The significant difference between this study and the previous work is that each floating cylinder in the array can experience multi-DOF (rather than single DOF) translational and rotational motions in the presence of regular and irregular incident waves. This paper is divided into the following parts: In Section 2, the analytical model of diffraction and radiation problems of the hydrodynamic interactions among truncated cylinders in the array was established, after which the formulas of velocity potential and motion amplitude of each DOF were derived. Then, Section 3 showed variations in the amplitude of each DOF in the array with dimensionless wavenumbers for different wave incidence angles and cylinder spacing, and gave the contour plots of the amplitude of free surface elevation for different wavenumbers. In Section 4, the oscillating amplitude of each cylinder, capture width and interaction factor of two WEC arrays were computed using a multi-DOF analysis model in this paper, after which we compared them with those of the single DOF model. In Section 5, the extensions to the situation of irregular waves were given. In Section 6, conclusions were summarized.

2. Mathematical models

This study was carried out in the context of time-harmonic linear water waves. As shown in Fig. 1(a), considering an array composed of N truncated cylinders that can experience multi-DOF translation and rotation in the presence of incident waves, there can be relative motions among cylinders (relative-motion-array). As shown in Fig. 1(b), each cylinder in the array is allowed to oscillate in surge, sway, heave, roll, and pitch modes, yaw motion is not considered because it does not produce hydrodynamic force in the ideal fluid. Meanwhile, each cylinder may have a different radius and draught. Göteman (2017) studied the case for arrays of cylinders with different sizes and topology but oscillating only in heave mode. As shown in Fig. 1(c), a global Cartesian coordinate system $OXYZ$ with (X, Y)-plane fixed on the undisturbed free surface and Z-axis pointing vertically upwards is introduced. In addition, for each cylinder, a local cylindrical coordinate system, $o_i r_i \theta_i z_i$, with its origin located at the intersection of the cylinder's axis and the undisturbed free surface and z_i-axis pointing vertically upwards is introduced.

The fluid is incompressible, inviscid and the flow is irrotational, the cylinder oscillates periodically with small amplitude in the presence of the incident linear water waves. Thus, the total velocity potential Φ can be expressed as

$$\Phi(X, Y, Z, t) = \mathrm{Re}\left\{\varphi(X, Y, Z)\, \mathrm{e}^{-\mathrm{i}\omega_0 t}\right\}, \tag{1}$$

where ω_0 is the angular frequency of the ambient incident wave; φ is the spatial factor, $\mathrm{e}^{-\mathrm{i}\omega_0 t}$ is the time factor and $\mathrm{i} = \sqrt{-1}$.

The fluid domain around each cylinder is divided into the exterior and core regions, as shown in Fig. 1(d), where the radius and draught of cylinder j are a_i and h_i and the water depth is d.

The total velocity potential $\varphi^{(j)}$ in the vicinity of cylinder j is represented by the total velocity potential in the exterior region $\varphi_E^{(j)}$ and the total velocity potential in core region $\varphi_C^{(j)}$. $\varphi_E^{(j)}$ can be further expressed as

$$\varphi_E^{(j)} = \varphi_I + \sum_{i=1}^{N} \varphi_{D-E}^{(i)} + \sum_{i=1}^{N} \sum_{s=1}^{5} \varphi_{Rs-E}^{(i)}, \tag{2}$$

where φ_I is the velocity potential of the ambient incident wave, $\varphi_{D-E}^{(i)}$ the diffraction potential in the exterior region of cylinder i; $\varphi_{Rs-E}^{(i)}$ the radiation potential of cylinder i oscillating in s mode. In order to solve the problem conveniently, $\varphi_{D-E}^{(i)}$ is divided into two parts $\varphi_{D0-E}^{(i)}$ and $\varphi_{D1-E}^{(i)}$: $\varphi_{D0-E}^{(i)}$, which is independent of oscillations of each cylinder, is the diffraction potential of cylinder i induced by the ambient incident wave acting on a fixed array; whereas $\varphi_{D1-E}^{(i)}$, related to the oscillations of every cylinder, is the diffraction potential of cylinder i induced by the radiated and diffracted waves of other cylinders except cylinder i when each cylinder undergoes five DOFs oscillations in the absence of the ambient incident wave. Then, Eq. (2) becomes

$$\varphi_E^{(j)} = \varphi_I + \sum_{i=1}^{N} \varphi_{D0-E}^{(i)} + \sum_{i=1}^{N} \sum_{s=1}^{5} \varphi_{Rs-E}^{(i)} + \sum_{i=1}^{N} \varphi_{D1-E}^{(i)}. \tag{3}$$

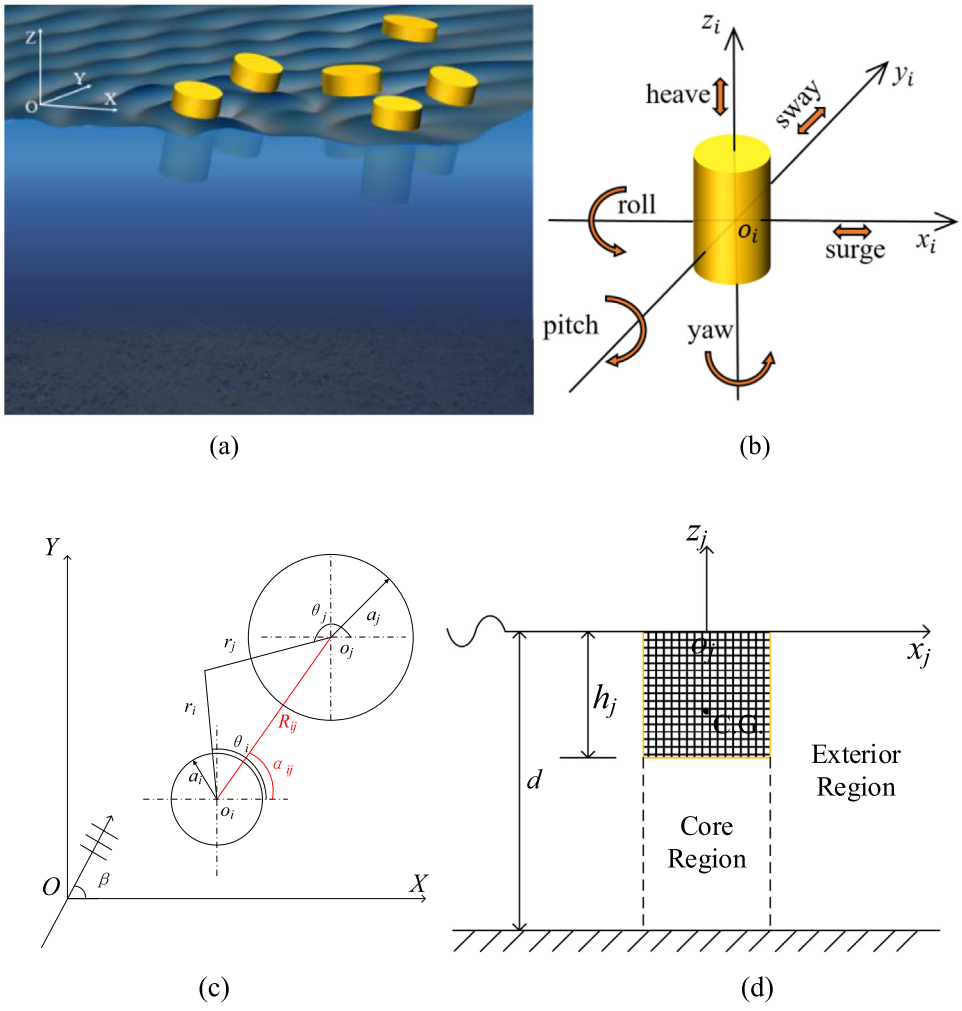

Fig. 1. Schematic showing (a) a cylinder array; (b) the multi-DOF motion of an isolated cylinder; (c) coordinate systems; (d) fluid domain division.

Let

$$\begin{aligned}\varphi_{ID-E}^{(j)} &= \varphi_I + \sum_{i=1}^{N} \varphi_{D0-E}^{(i)},\\ \varphi_{RD-E}^{(j)} &= \sum_{i=1}^{N}\sum_{s=1}^{5} \varphi_{Rs-E}^{(i)} + \sum_{i=1}^{N} \varphi_{D1-E}^{(i)},\end{aligned} \tag{4}$$

Consequently,

$$\varphi_E^{(j)} = \varphi_{ID-E}^{(j)} + \varphi_{RD-E}^{(j)}, \tag{5}$$

where $\varphi_{ID-E}^{(j)}$ is the velocity potential in the exterior region of cylinder j in the presence of incident waves, which is the sum of the ambient incident potential and the resulting diffraction potential of each cylinder, the subscript *ID* indicates incidence–diffraction. $\varphi_{RD-E}^{(j)}$ is the velocity potential in the exterior region of cylinder j when each cylinder in the array performs five DOF oscillations with different amplitudes, which is the sum of the radiation potential of each cylinder and the resulting diffraction potentials, and subscript *RD* indicates radiation–diffraction.

Similarly, the velocity potential in the core region can also be divided into $\varphi_{ID-C}^{(j)}$ and $\varphi_{RD-C}^{(j)}$:

$$\varphi_C^{(j)} = \varphi_{ID-C}^{(j)} + \varphi_{RD-C}^{(j)}, \tag{6}$$

where $\varphi_{ID-C}^{(j)}$ is the velocity potential in the core region in the presence of the ambient incident wave; $\varphi_{RD-C}^{(j)}$ is the velocity potential in the core region in the absence of the ambient incident wave, induced by radiation (due to oscillations of cylinders) and the diffraction of radiated waves.

In the following, Section 2.1 is about the diffraction problem of ambient incident waves for fixed truncated cylinders, with the formulas listed in Appendix A using symbols in this paper, with which wave exciting forces and moments are presented in Section 2.3. Section 2.2 solved the radiation–diffraction problem for arrays of independently oscillating truncated cylinders, with which radiation–diffraction forces and moments are given in Section 2.3. Considering hydrodynamic forces and other forces acting on the cylinder, the equations of motion of arrays of truncated cylinders in which each cylinder is allowed to oscillate with five DOFs are given in Section 2.3.

2.1. The velocity potential for diffraction problems of a truncated-cylinder array

As mentioned above, the total velocity potential in the vicinity of a cylinder in an array is divided into two parts: one is the velocity potential for diffraction problems in the presence of the ambient incident wave, and the other is the velocity potential for radiation–diffraction problems, in which cylinders oscillate with different amplitudes in the absence of the ambient incident wave. This section follows the method of Kagemoto and Yue (1986) and Yilmaz (1998) to solve the diffraction problem of a truncated-cylinder array. Some main formulas used in obtaining the velocity potentials $\varphi_{ID-E}^{(j)}$ and $\varphi_{ID-C}^{(j)}$ of the diffraction problem in this study are listed in Appendix A.

2.2. The velocity potential for radiation–diffraction problems when each cylinder in a truncated-cylinder array oscillates with different amplitudes

In this study, the radiation–diffraction velocity potential induced by the array motion is expressed by the linear combination of the unknown oscillation amplitudes of each cylinder, after which the radiation–diffraction hydrodynamic forces expressed by unknown oscillation amplitudes are obtained. Considering the wave exciting forces, radiation–diffraction hydrodynamic forces, inertial forces, restoring forces, and other damping forces (damping forces other than radiation damping forces), motion equations of every cylinder in the array can be obtained, after which the amplitude of each degree of freedom of each cylinder can be obtained by solving the simultaneous equations. Once the oscillation amplitudes are obtained, the radiation–diffraction velocity potential of the array can be obtained at the same time.

In this section, the radiation–diffraction problem of a truncated-cylinder array, in the absence of the ambient incident wave, is studied when each cylinder in the array performs five DOF oscillations with different amplitudes.

First, we study how to express the velocity potentials $\varphi_{RD-E}^{(j)}$ and $\varphi_{RD-C}^{(j)}$ of the radiation–diffraction problem using a linear combination of the unknown oscillation amplitudes of each cylinder.

Each cylinder in the array oscillates periodically at frequency ω_0, and its displacement is:

$$\Xi_s^{(i)}(t) = \mathrm{Re}\left\{\zeta_s^{(i)} \mathrm{e}^{-\mathrm{i}\omega_0 t}\right\}, \tag{7}$$

where $\zeta_s^{(i)}$ is the complex amplitude of cylinder i in the direction of the sth degree of freedom, and the corresponding velocity is

$$\dot{\Xi}_s^i(t) = \mathrm{Re}\left\{-\mathrm{i}\omega_0 \zeta_s^{(i)} \mathrm{e}^{-\mathrm{i}\omega_0 t}\right\}. \tag{8}$$

In the coordinate system $o_i r_i \theta_i z_i$, the radiation potential $\varphi_{Rs-E}^{(i)}$ in the exterior region, generated by the oscillation of cylindrical i with amplitude $\zeta_s^{(i)}$, can be written as

$$\varphi_{Rs-E}^{(i)} = -\mathrm{i}\omega_0 \zeta_s^{(i)} \sum_{m=-\infty}^{\infty} \left[R_{0ms}^{(i)} Z_0(z) H_m(k_0 r_i) + \sum_{n=1}^{\infty} R_{nms}^{(i)} Z_n(z) K_m(k_n r_i) \right] \mathrm{e}^{\mathrm{i}m\theta_i}, \tag{9}$$

with $R_{nms}^{(i)}$ being the radiation characteristics of an isolated truncated cylinder:

$$R_{nms}^{(i)} = \begin{cases} \dfrac{D_{R0m}^s \cosh k_0 d}{H_m'(k_0 a_i) N_0^{1/2}}, & n = 0, \\ \dfrac{D_{Rnm}^s}{K_m'(k_n a_i) N_n^{1/2}}, & n > 0, \end{cases} \tag{10}$$

where coefficients $D_{R_{nm}^s}$ is given in Appendix B, N_0 and N_n are:

$$N_0 = \frac{1}{2}\left(1 + \frac{\sin h2k_0 d}{2k_0 d}\right), \quad N_n = \frac{1}{2}\left(1 + \frac{\sin 2k_n d}{2k_n d}\right). \tag{11}$$

Eq. (9) can be written in the form of a matrix and further represented in the coordinate system $o_j r_j \theta_j z_j$ using the coordinate transformation matrix $\mathbf{T_{ij}}$:

$$\varphi_{Rs-E}^{(i)} = -\mathrm{i}\omega_0 \zeta_s^{(i)} \mathbf{R_{is}}^T \boldsymbol{\psi}_\mathbf{i}^{\mathbf{D-E}} = -\mathrm{i}\omega_0 \zeta_s^{(i)} \mathbf{R_{is}}^T \mathbf{T_{ij}} \boldsymbol{\psi}_\mathbf{j}^{\mathbf{I}}. \tag{12}$$

When each cylinder performs DOF oscillations, the diffraction potential in the exterior region of cylinder i induced by the radiated and diffracted waves of other cylinders in the array except cylinder i can be written as

$$\varphi_{D1-E}^{(i)} = \sum_{m=-\infty}^{\infty} \left[A_{R0m}^{(i)} Z_0(z) H_m(k_0 r_i) + \sum_{n=1}^{\infty} A_{Rnm}^{(i)} Z_n(z) K_m(k_n r_i) \right] \mathrm{e}^{\mathrm{i}m\theta_i}. \tag{13}$$

Similar to Eqs. (12), (13) can also be rewritten in the form of a matrix as

$$\varphi_{D1-E}^{(i)} = \mathbf{A_{Ri}}^T \boldsymbol{\psi}_\mathbf{i}^{\mathbf{D-E}} = \mathbf{A_{Ri}}^T \mathbf{T_{ij}} \boldsymbol{\psi}_\mathbf{j}^{\mathbf{I}}, \tag{14}$$

where the coefficient column vector $\mathbf{A_{Ri}}$ is to be determined.

The total incident waves of cylinder j consist of the radiated and diffracted waves emitted from other cylinders:

$$\begin{aligned} &\sum_{i=1,i\neq j}^{N} \varphi_{Rs-E}^{(i)}|_j + \sum_{i=1,i\neq j}^{N} \varphi_{D1-E}^{(i)}|_j \\ &= \sum_{i=1,i\neq j}^{N} \sum_{s=1}^{5} \left(-\mathrm{i}\omega_0 \zeta_s^{(i)} \mathbf{R_{is}}^T\right) \mathbf{T_{ij}} \boldsymbol{\psi}_\mathbf{j}^{\mathbf{I}} + \sum_{i=1,i\neq j}^{N} \mathbf{A_{Ri}}^T \mathbf{T_{ij}} \boldsymbol{\psi}_\mathbf{j}^{\mathbf{I}} \\ &= \sum_{i=1,i\neq j}^{N} \left[\sum_{s=1}^{5} \left(-\mathrm{i}\omega_0 \zeta_s^{(i)} \mathbf{R_{is}}^T\right) + \mathbf{A_{Ri}}^T \right] \mathbf{T_{ij}} \boldsymbol{\psi}_\mathbf{j}^{\mathbf{I}}. \end{aligned} \tag{15}$$

Thus, the total radiated waves in the vicinity of cylinder j can be related by its isolated-body inherent diffraction transfer matrix $\mathbf{B_j^E}$ (Kagemoto and Yue, 1986):

$$\mathbf{A_{Rj}} = \mathbf{B_j^E} \sum_{i=1,i\neq j}^{N} \mathbf{T_{ij}}^T \left[\sum_{s=1}^{5} \left(-\mathrm{i}\omega_0 \zeta_s^{(i)} \mathbf{R_{is}}\right) + \mathbf{A_{Ri}} \right], \quad j = 1, 2, \ldots, N. \tag{16}$$

where $\mathbf{B_j^E}$ is given in Appendix A. The unknown coefficient vector $\mathbf{A_{Rj}}$ can be obtained by solving Eq. (16). By combining the equations of all $\mathbf{A_{Rj}}$ as shown above, we can get

$$\mathbf{A_R} = -\mathrm{i}\omega_0 \sum_{s=1}^{5} [\mathbf{E} - \mathbf{BT}]^{-1} \mathbf{BTR_s} \boldsymbol{\zeta}_\mathbf{s}, \tag{17}$$

where

$$\mathbf{A_R} = \left[\mathbf{A_{R1}}^T, \mathbf{A_{R2}}^T, \ldots, \mathbf{A_{Rj}}^T, \ldots, \mathbf{A_{R(N-1)}}^T, \mathbf{A_{RN}}^T\right]^T, \tag{18}$$

$$\mathbf{B} = \begin{bmatrix} \mathbf{B_1^E} & 0 & \cdots & 0 \\ 0 & \mathbf{B_2^E} & \cdots & 0 \\ \vdots & \vdots & & \vdots \\ 0 & 0 & \cdots & \mathbf{B_N^E} \end{bmatrix}, \tag{19}$$

$$\mathbf{T} = \begin{bmatrix} 0 & \mathbf{T_{21}}^T & \cdots & \mathbf{T_{N1}}^T \\ \mathbf{T_{12}}^T & 0 & & \vdots \\ \vdots & & 0 & \mathbf{T_{N(N-1)}}^T \\ \mathbf{T_{1N}}^T & \cdots & \mathbf{T_{(N-1)N}}^T & 0 \end{bmatrix}, \tag{20}$$

$$\mathbf{R_s} = \begin{bmatrix} \mathbf{R_{1s}} & 0 & \cdots & 0 \\ 0 & \mathbf{R_{2s}} & \cdots & 0 \\ \vdots & \vdots & & \vdots \\ 0 & 0 & \cdots & \mathbf{R_{Ns}} \end{bmatrix}, \tag{21}$$

$$\boldsymbol{\zeta_s} = \left[\zeta_s^{(1)},\ \zeta_s^{(2)},\ \ldots,\ \zeta_s^{(j)},\ \ldots,\ \zeta_s^{(N-1)},\ \zeta_s^{(N)}\right]^T, \tag{22}$$

In the calculation, the infinite series in Eq. (13) is truncated into the sum of finite terms with upper bounds of summation m_0 and n_0. $\mathbf{A_R}$ is a $N(n_0{+}1)(2m_0{+}1)$-by-1 matrix with N row partitions (matrix partitioned into N blocks by rows, each block being a column vector with $(n_0{+}1)(2m_0{+}1)$ entries); $\mathbf{E}$ is the identity matrix of order $N(n_0{+}1)(2m_0{+}1)$ with N row partitions and N column partitions; $\mathbf{B}$ and $\mathbf{T}$ are two square matrices of order $N(n_0{+}1)(2m_0{+}1)$ with N row partitions and N column partitions. $\mathbf{R_s}$ is a $N(n_0{+}1)(2m_0{+}1)$-by-N matrix with N row partitions and N column partitions. $\boldsymbol{\zeta_s}$ is a column vector with N entries.

$[\mathbf{E}-\mathbf{BT}]^{-1}\mathbf{BTR_s}$ is a $N(n_0{+}1)(2m_0{+}1)$-by-N matrix, which can be partitioned into N^2 submatrices as follows:

$$[\mathbf{E}-\mathbf{BT}]^{-1}\mathbf{BTR_s} = \begin{bmatrix} \boldsymbol{\kappa}_{\mathbf{11s}} & \cdots & \boldsymbol{\kappa}_{\mathbf{1ks}} & \cdots & \boldsymbol{\kappa}_{\mathbf{1Ns}} \\ \vdots & & \vdots & & \vdots \\ \boldsymbol{\kappa}_{\mathbf{j1s}} & \cdots & \boldsymbol{\kappa}_{\mathbf{jks}} & \cdots & \boldsymbol{\kappa}_{\mathbf{jNs}} \\ \vdots & & \vdots & & \vdots \\ \boldsymbol{\kappa}_{\mathbf{N1s}} & \cdots & \boldsymbol{\kappa}_{\mathbf{Nks}} & \cdots & \boldsymbol{\kappa}_{\mathbf{NNs}} \end{bmatrix}, \tag{23}$$

Each submatrix $\boldsymbol{\kappa}_{\mathbf{jks}}$ is a column vector with $(n_0{+}1)(2m_0{+}1)$ entries. According to Eq. (17), Eq. (18), Eq. (22), and Eq. (23), we can obtain the expression below

$$\mathbf{A_{Rj}} = -\mathrm{i}\omega_0 \sum_{s=1}^{5}\sum_{k=1}^{N} \boldsymbol{\kappa}_{\mathbf{jks}}\zeta_s^{(k)}. \tag{24}$$

Therefore, for the radiation–diffraction problem, the total velocity potential in the exterior region of cylinder j can be obtained, as shown below

$$\begin{aligned}
\varphi_{RD-E}^{(j)} &= \left[\sum_{s=1}^{5}\left(-\mathrm{i}\omega_0\zeta_s^{(j)}\mathbf{R_{js}}^T\right) + \mathbf{A_{Rj}}^T\right]\boldsymbol{\psi}_\mathbf{j}^{\mathbf{D-E}} + \sum_{i=1,i\neq j}^{N}\left[\sum_{s=1}^{5}\left(-\mathrm{i}\omega_0\zeta_s^{(i)}\mathbf{R_{is}}^T\right) + \mathbf{A_{Ri}}^T\right]\mathbf{T_{ij}}\boldsymbol{\psi}_\mathbf{j}^{\mathbf{I}} \\
&= \left[\sum_{s=1}^{5}\left(-\mathrm{i}\omega_0\zeta_s^{(j)}\mathbf{R_{js}}^T\right) - \mathrm{i}\omega_0\sum_{s=1}^{5}\sum_{k=1}^{N}\zeta_s^{(k)}\boldsymbol{\kappa}_{\mathbf{jks}}^T\right]\boldsymbol{\psi}_\mathbf{j}^{\mathbf{D-E}} \\
&\quad + \sum_{i=1,i\neq j}^{N}\left[\sum_{s=1}^{5}\left(-\mathrm{i}\omega_0\zeta_s^{(i)}\mathbf{R_{is}}^T\right) - \mathrm{i}\omega_0\sum_{s=1}^{5}\sum_{k=1}^{N}\zeta_s^{(k)}\boldsymbol{\kappa}_{\mathbf{iks}}^T\right]\mathbf{T_{ij}}\boldsymbol{\psi}_\mathbf{j}^{\mathbf{I}} \\
&= -\mathrm{i}\omega_0\sum_{s=1}^{5}\left\{\zeta_s^{(j)}\left[\left(\mathbf{R_{js}}^T + \boldsymbol{\kappa}_{\mathbf{jjs}}^T\right)\boldsymbol{\psi}_\mathbf{j}^{\mathbf{D-E}} + \sum_{i=1,i\neq j}^{N}\boldsymbol{\kappa}_{\mathbf{ijs}}^T\mathbf{T_{ij}}\boldsymbol{\psi}_\mathbf{j}^{\mathbf{I}}\right]\right. \\
&\quad \left. + \sum_{k=1,k\neq j}^{N}\zeta_s^{(k)}\left[\boldsymbol{\kappa}_{\mathbf{jks}}^T\boldsymbol{\psi}_\mathbf{j}^{\mathbf{D-E}} + \left(\mathbf{R_{ks}}^T\mathbf{T_{kj}}\boldsymbol{\psi}_\mathbf{j}^{\mathbf{I}} + \sum_{i=1,i\neq j}^{N}\boldsymbol{\kappa}_{\mathbf{iks}}^T\mathbf{T_{ij}}\boldsymbol{\psi}_\mathbf{j}^{\mathbf{I}}\right)\right]\right\} \\
&= -\mathrm{i}\omega_0\sum_{s=1}^{5}\left(\zeta_s^{(j)}\varphi_{RD-Es}^{(jj)} + \sum_{k=1,k\neq j}^{N}\zeta_s^{(k)}\varphi_{RD-Es}^{(jk)}\right),
\end{aligned} \tag{25}$$

where

$$\begin{aligned}
\varphi_{RD-Es}^{(jj)} &= \left(\mathbf{R_{js}}^T + \boldsymbol{\kappa}_{\mathbf{jjs}}^T\right)\boldsymbol{\psi}_\mathbf{j}^{\mathbf{D-E}} + \sum_{i=1,i\neq j}^{N}\boldsymbol{\kappa}_{\mathbf{ijs}}^T\mathbf{T_{ij}}\boldsymbol{\psi}_\mathbf{j}^{\mathbf{I}}, \\
\varphi_{RD-Es}^{(jk)} &= \boldsymbol{\kappa}_{\mathbf{jks}}^T\boldsymbol{\psi}_\mathbf{j}^{\mathbf{D-E}} + \left(\mathbf{R_{ks}}^T\mathbf{T_{kj}}\boldsymbol{\psi}_\mathbf{j}^{\mathbf{I}} + \sum_{i=1,i\neq j}^{N}\boldsymbol{\kappa}_{\mathbf{iks}}^T\mathbf{T_{ij}}\boldsymbol{\psi}_\mathbf{j}^{\mathbf{I}}\right).
\end{aligned} \tag{26}$$

The total velocity potential in the core region of cylinder j can also be obtained, as shown below

$$\begin{aligned}
\varphi_{RD-C}^{(j)} &= \sum_{s=1}^{5}\left[-\mathrm{i}\omega_0\zeta_s^{(j)}\varphi_{Rs-C}^{(j)}(r_j,\theta_j,z)\right] + \left\{\sum_{i=1,i\neq j}^{N}\left[\sum_{s=1}^{5}\left(-\mathrm{i}\omega_0\zeta_s^{(i)}\mathbf{R_{is}}^T\right)+\mathbf{A_{Ri}}^T\right]\mathbf{T_{ij}}\right\}\left(\mathbf{B_j^C}\right)^T\boldsymbol{\psi}_\mathbf{j}^{\mathbf{D-C}} \\
&= -\mathrm{i}\omega_0\sum_{s=1}^{5}\left\{\zeta_s^{(j)}\varphi_{Rs-C}^{(j)}(r_j,\theta_j,z)+\sum_{i=1,i\neq j}^{N}\left[\zeta_s^{(i)}\mathbf{R_{is}}^T+\sum_{k=1}^{N}\zeta_s^{(k)}\boldsymbol{\kappa}_{\mathbf{iks}}{}^T\right]\mathbf{T_{ij}}\left(\mathbf{B_j^C}\right)^T\boldsymbol{\psi}_\mathbf{j}^{\mathbf{D-C}}\right\} \\
&= -\mathrm{i}\omega_0\sum_{s=1}^{5}\left\{\zeta_s^{(j)}\left[\varphi_{Rs-C}^{(j)}(r_j,\theta_j,z)+\sum_{i=1,i\neq j}^{N}\boldsymbol{\kappa}_{\mathbf{ijs}}{}^T\mathbf{T_{ij}}\left(\mathbf{B_j^C}\right)^T\boldsymbol{\psi}_\mathbf{j}^{\mathbf{D-C}}\right]\right. \\
&\quad \left.+\sum_{k=1,\mathrm{k}\neq j}^{N}\zeta_s^{(k)}\left(\mathbf{R_{ks}}^T\mathbf{T_{kj}}\left(\mathbf{B_j^C}\right)^T\boldsymbol{\psi}_\mathbf{j}^{\mathbf{D-C}}+\sum_{i=1,i\neq j}^{N}\boldsymbol{\kappa}_{\mathbf{iks}}{}^T\mathbf{T_{ij}}\left(\mathbf{B_j^C}\right)^T\boldsymbol{\psi}_\mathbf{j}^{\mathbf{D-C}}\right)\right\} \\
&= -\mathrm{i}\omega_0\sum_{s=1}^{5}\left(\zeta_s^{(j)}\varphi_{RD-Cs}^{(jj)}+\sum_{k=1,\mathrm{k}\neq j}^{N}\zeta_s^{(k)}\varphi_{RD-Cs}^{(jk)}\right),
\end{aligned} \tag{27}$$

where

$$\begin{aligned}
\varphi_{RD-Cs}^{(jj)} &= \varphi_{Rs-C}^{(j)}\left(r_j,\,\theta_j,\,z\right)+\sum_{i=1,i\neq j}^{N}\boldsymbol{\kappa}_{\mathbf{ijs}}{}^T\mathbf{T_{ij}}\left(\mathbf{B_j^C}\right)^T\boldsymbol{\psi}_\mathbf{j}^{\mathbf{D-C}}, \\
\varphi_{RD-Cs}^{(jk)} &= \mathbf{R_{ks}}{}^T\mathbf{T_{kj}}\left(\mathbf{B_j^C}\right)^T\boldsymbol{\psi}_\mathbf{j}^{\mathbf{D-C}}+\sum_{i=1,i\neq j}^{N}\boldsymbol{\kappa}_{\mathbf{iks}}{}^T\mathbf{T_{ij}}\left(\mathbf{B_j^C}\right)^T\boldsymbol{\psi}_\mathbf{j}^{\mathbf{D-C}},
\end{aligned} \tag{28}$$

and $\varphi_{Rs-C}^{(j)}$ is the radiation potential for an isolated cylinder in the core region of cylinder j, defined as

$$\varphi_{Rs-C}^{(j)}(r_j,\,\theta_j,\,z)=\sum_{m=-\infty}^{\infty}\left\{\begin{array}{l}\frac{C_{R0m}^s}{2}\left(\frac{r_j}{a_j}\right)^{|m|}+ \\ \sum_{p=1}^{\infty}C_{Rpm}^s\frac{I_m\left(\frac{p\pi r_j}{d-h_j}\right)}{I_m\left(\frac{p\pi a_j}{d-h_j}\right)}\cos\left[\frac{p\pi\,(z+d)}{d-h_j}\right]+\Lambda_s\lambda_{ms}\end{array}\right\}\mathrm{e}^{\mathrm{i}m\theta_j}, \tag{29}$$

where coefficients C_{Rpm}^s, Λ_s and λ_{ms} are defined in detail in Appendix B.

It is evident from Eqs. (17), (25), and (27) that for the radiation–diffraction problem of an array, the linear combination of the amplitudes of each DOF $\zeta_s^{(i)}$ can represent the diffraction potential coefficient vector $\mathbf{A_{Rj}}$, and further represent the total velocity potentials $\varphi_{RD-E}^{(j)}$ and $\varphi_{RD-C}^{(j)}$. Based on this result, the amplitude $\zeta_s^{(i)}$ can be subsequently solved using the dynamic equations for each cylinder, which will be described in detail in the next section.

2.3. The hydrodynamic forces/moments and oscillation amplitudes of each cylinder in a truncated-cylinder array

As shown in Eqs. (5) and (6), once $\varphi_{ID-E}^{(j)}$, $\varphi_{ID-C}^{(j)}$, $\varphi_{RD-E}^{(j)}$, and $\varphi_{RD-C}^{(j)}$ have been obtained, the total velocity potentials in the exterior region $\varphi_E^{(j)}$ and the core region $\varphi_C^{(j)}$ can also be obtained. Therefore, the spatial factor of hydrodynamic pressure on cylinder j becomes

$$\mathcal{P}^{(j)}=\mathrm{i}\rho\omega\varphi^{(j)}, \tag{30}$$

Subsequently, the total hydrodynamic forces and moments on cylinder j can be obtained by integrating the pressure over its wet surface S, resulting in its spatial factor $\mathcal{F}_{Hp}^{(j)}$, as shown below

$$\mathcal{F}_{Hp}^{(j)}=\left\{\begin{array}{ll}\int\mathcal{P}^{(j)}\mathbf{n}dS, & p=1,\,2,\,3, \\ \int\mathcal{P}^{(j)}\left(\mathbf{r}\times\mathbf{n}\right)dS, & p=4,\,5,\end{array}\right. \tag{31}$$

where $\mathbf{r}$ is the position vector pointing from the center of mass to the integrating point and $\mathbf{n}$ is the unit normal vector of wet surface pointing into the body:

$$\mathbf{n}=\left\{\begin{array}{ll}\left(-\cos\theta_j,-\sin\theta_j,0\right), & \textit{lateral surface}, \\ (0,0,1), & \textit{bottom surface}.\end{array}\right. \tag{32}$$

Substituting Eqs. (25) and (27) into Eqs. (30) and (31), we can get

$$\mathcal{F}_{Hp}^{(j)} = \mathcal{F}_{IDp}^{(j)} + \mathcal{F}_{RDp}^{(j)} = \mathcal{F}_{IDp}^{(j)} + \sum_{s=1}^{5}\sum_{i=1}^{N} F_{RDps}^{(ji)}\zeta_s^i, \tag{33}$$

where the exciting force/moment $\mathcal{F}_{IDp}^{(j)}$ in each direction on cylinder j is defined as follows: Surge exciting force:

$$\mathcal{F}_{ID1}^{(j)} = -\mathrm{i}\omega_0\rho\int_0^{2\pi}\int_{-h}^{0}\varphi_{ID-E}^{(j)}\Big|_{r=a_j}\cos\theta_j a_j d\theta_j dz, \tag{34}$$

Sway exciting force:

$$\mathcal{F}_{ID2}^{(j)} = -\mathrm{i}\omega_0\rho\int_0^{2\pi}\int_{-h}^{0}\varphi_{ID-E}^{(j)}\Big|_{r=a_j}\sin\theta_j a_j d\theta_j dz, \tag{35}$$

Heave exciting force:

$$\mathcal{F}_{ID3}^{(j)} = \mathrm{i}\omega_0\rho\int_0^{2\pi}\int_{0}^{a}\varphi_{ID-C}^{(j)}\Big|_{z=-h_j} r_j dr_j d\theta_j, \tag{36}$$

Roll exciting moment:

$$\mathcal{F}_{ID4}^{(j)} = \mathrm{i}\omega_0\rho\int_0^{2\pi}\int_{0}^{a}\varphi_{ID-C}^{(j)}\Big|_{z=-h_j} r_j\sin\theta_j r_j dr_j d\theta_j + \mathrm{i}\omega_0\rho\int_0^{2\pi}\int_{-h}^{0}\varphi_{ID-E}^{(j)}\Big|_{r=a}\left(z-\bar{z}_j\right)\sin\theta_j a_j d\theta_j dz, \tag{37}$$

Pitch exciting moment:

$$\mathcal{F}_{ID5}^{(j)} = -\mathrm{i}\omega_0\rho\int_0^{2\pi}\int_{0}^{a}\varphi_{ID-C}^{(j)}\Big|_{z=-h_j} r_j\cos\theta_j r_j dr_j d\theta_j - \mathrm{i}\omega_0\rho\int_0^{2\pi}\int_{-h}^{0}\varphi_{ID-E}^{(j)}\Big|_{r=a_j}\left(z-\bar{z}_j\right)\cos\theta_j a_j d\theta_j dz, \tag{38}$$

The radiation–diffraction hydrodynamic force/moment $\mathcal{F}_{RDp}^{(j)}$ on cylinder j, induced by the oscillations of all cylinders in the array, is defined as follows:
Radiation–diffraction hydrodynamic force in the surge direction:

$$\begin{aligned}
&\mathcal{F}_{RD1}^{(j)} = \mathrm{i}\omega_0\rho\int_0^{2\pi}\int_{-h_j}^{0}\varphi_{RD-E}^{(j)}\Big|_{r=a_j}\left(-\cos\theta_j\right)a_j d\theta_j dz\\
&= \mathrm{i}\omega_0\rho\int_0^{2\pi}\int_{-h_j}^{0}\mathrm{i}\omega_0\sum_{s=1}^{5}\left(\zeta_s^{(j)}\varphi_{RD-Es}^{(jj)} + \sum_{k=1,k\neq j}^{N}\zeta_s^{(k)}\varphi_{RD-Es}^{(jk)}\right)\Big|_{r=a_j}\cos\theta_j a_j d\theta_j dz\\
&= \sum_{s=1}^{5}\left[\zeta_s^{(j)}\left(-{\omega_0}^2\rho\int_0^{2\pi}\int_{-h_j}^{0}\varphi_{RD-Es}^{(jj)}\Big|_{r=a_j}\cos\theta_j a_j d\theta_j dz\right) + \sum_{k=1,k\neq j}^{N}\zeta_s^{(k)}\left(-{\omega_0}^2\rho\int_0^{2\pi}\int_{-h_j}^{0}\varphi_{RD-Es}^{(jk)}\Big|_{r=a_j}\cos\theta_j a_j d\theta_j dz\right)\right]\\
&= \sum_{s=1}^{5}\left(\zeta_s^{(j)}F_{RD1s}^{(jj)} + \sum_{k=1,k\neq j}^{N}\zeta_s^{(k)}F_{RD1s}^{(jk)}\right) = \sum_{s=1}^{5}\sum_{i=1}^{N}F_{RD1s}^{(ji)}\zeta_s^i,
\end{aligned} \tag{39}$$

Radiation–diffraction hydrodynamic force in the sway direction:

$$\begin{aligned}
&\mathcal{F}_{RD2}^{(j)} = \mathrm{i}\omega_0\rho\int_0^{2\pi}\int_{-h_j}^{0}\varphi_{RD-E}^{(j)}\Big|_{r=a_j}\left(-\sin\theta_j\right)a_j d\theta_j dz\\
&= \mathrm{i}\omega_0\rho\int_0^{2\pi}\int_{-h_j}^{0}\mathrm{i}\omega_0\sum_{s=1}^{5}\left(\zeta_s^{(j)}\varphi_{RD-Es}^{(jj)} + \sum_{k=1,k\neq j}^{N}\zeta_s^{(k)}\varphi_{RD-Es}^{(jk)}\right)\Big|_{r=a_j}\sin\theta_j a_j d\theta_j dz\\
&= \sum_{s=1}^{5}\left[\zeta_s^{(j)}\left(-{\omega_0}^2\rho\int_0^{2\pi}\int_{-h_j}^{0}\varphi_{RD-Es}^{(jj)}\Big|_{r=a_j}\sin\theta_j a_j d\theta_j dz\right) + \sum_{k=1,k\neq j}^{N}\zeta_s^{(k)}\left(-{\omega_0}^2\rho\int_0^{2\pi}\int_{-h_j}^{0}\varphi_{RD-Es}^{(jk)}\Big|_{r=a_j}\sin\theta_j a_j d\theta_j dz\right)\right]\\
&= \sum_{s=1}^{5}\left(\zeta_s^{(j)}F_{RD2s}^{(jj)} + \sum_{k=1,k\neq j}^{N}\zeta_s^{(k)}F_{RD2s}^{(jk)}\right) = \sum_{s=1}^{5}\sum_{i=1}^{N}F_{RD2s}^{(ji)}\zeta_s^i,
\end{aligned} \tag{40}$$

Radiation–diffraction hydrodynamic force in the heave direction:

$$\begin{aligned}
\mathcal{F}_{RD3}^{(j)} &= \mathrm{i}\omega_0\rho\int_0^{2\pi}\int_0^{a_j}\varphi_{RD-C}^{(j)}\Big|_{z=-h_j} r_j dr_j d\theta_j \\
&= -\mathrm{i}\omega_0\rho\int_0^{2\pi}\int_0^{a_j}\mathrm{i}\omega_0\sum_{s=1}^{5}\left(\zeta_s^{(j)}\varphi_{RD-Cs}^{(jj)}+\sum_{k=1,\mathrm{k}\neq j}^{N}\zeta_s^{(k)}\varphi_{RD-Cs}^{(jk)}\right)\Bigg|_{z=-h_j} r_j dr_j d\theta_j \\
&= \sum_{s=1}^{5}\left[\zeta_s^{(j)}\left(\omega_0{}^2\rho\int_0^{2\pi}\int_0^{a_j}\varphi_{RD-Cs}^{(jj)}\Big|_{z=-h_j} r_j dr_j d\theta_j\right)+\sum_{k=1,k\neq j}^{N}\zeta_s^{(k)}\left(\omega_0{}^2\rho\int_0^{2\pi}\int_0^{a_j}\varphi_{RD-Cs}^{(jk)}\Big|_{z=-h_j} r_j dr_j d\theta_j\right)\right] \\
&= \sum_{s=1}^{5}\left(\zeta_s^{(j)}F_{RD3s}^{(jj)}+\sum_{k=1,k\neq j}^{N}\zeta_s^{(k)}F_{RD3s}^{(jk)}\right)=\sum_{s=1}^{5}\sum_{i=1}^{N}F_{RD3s}^{(ji)}\zeta_s^{i},
\end{aligned} \tag{41}$$

Radiation–diffraction hydrodynamic moment in the roll direction:

$$\begin{aligned}
\mathcal{F}_{RD4}^{(j)} &= \mathrm{i}\omega_0\rho\left(\int_0^{2\pi}\int_0^{a_j}\varphi_{RD-C}^{j}\,|_{z=-h_j}\, r_j{}^2\sin\theta_j dr_j d\theta_j+\int_0^{2\pi}\int_{-h}^{0}\varphi_{RD-E}^{j}\,|_{r=a_j}\,(z-\overline{z}_j)\,a_j\sin\theta_j d\theta_j dz\right) \\
&= -\mathrm{i}\omega_0\rho\left[\int_0^{2\pi}\int_0^{a_j}\mathrm{i}\omega_0\sum_{s=1}^{5}\left(\zeta_s^{(j)}\varphi_{RD-Cs}^{(jj)}+\sum_{k=1,\mathrm{k}\neq j}^{N}\zeta_s^{(k)}\varphi_{RD-Cs}^{(jk)}\right)\Bigg|_{z=-h_j} r_j{}^2\sin\theta_j dr_j d\theta_j\right. \\
&\quad\left.+\int_0^{2\pi}\int_{-h_j}^{0}\mathrm{i}\omega_0\sum_{s=1}^{5}\left(\zeta_s^{(j)}\varphi_{RD-Es}^{(jj)}+\sum_{k=1,\mathrm{k}\neq j}^{N}\zeta_s^{(k)}\varphi_{RD-Es}^{(jk)}\right)\Bigg|_{r=a_j}(z-\overline{z}_j)\,a_j\sin\theta_j d\theta_j dz\right] \\
&= \sum_{s=1}^{5}\left[\zeta_s^{(j)}\left(\omega_0{}^2\rho\int_0^{2\pi}\int_0^{a_j}\varphi_{RD-Cs}^{(jj)}\Big|_{z=-h_j} r_j{}^2\sin\theta_j dr_j d\theta_j+\omega_0{}^2\rho\int_0^{2\pi}\int_{-h_j}^{0}\varphi_{RD-Es}^{(jj)}\Big|_{r=a_j}(z-\overline{z}_j)\,a_j\sin\theta_j d\theta_j dz\right)\right. \\
&\quad\left.+\sum_{k=1,k\neq j}^{N}\zeta_s^{(k)}\left(\omega_0{}^2\rho\int_0^{2\pi}\int_0^{a_j}\varphi_{RD-Cs}^{(jk)}\Big|_{z=-h_j} r_j{}^2\sin\theta_j dr_j d\theta_j+\omega_0{}^2\rho\int_0^{2\pi}\int_{-h_j}^{0}\varphi_{RD-Es}^{(jk)}\Big|_{r=a_j}(z-\overline{z}_j)\,a_j\sin\theta_j d\theta_j dz\right)\right] \\
&= \sum_{s=1}^{5}\left(\zeta_s^{(j)}F_{RD4s}^{(jj)}+\sum_{k=1,k\neq j}^{N}\zeta_s^{(k)}F_{RD4s}^{(jk)}\right)=\sum_{s=1}^{5}\sum_{i=1}^{N}F_{RD4s}^{(ji)}\zeta_s^{i},
\end{aligned} \tag{42}$$

Radiation–diffraction hydrodynamic moment in the pitch direction:

$$\begin{aligned}
\mathcal{F}_{RD5}^{(j)} &= \mathrm{i}\omega_0\rho\left(-\int_0^{2\pi}\int_0^{a_j}\varphi_{RD-C}^{j}\,|_{z=-h_j}\, r_j{}^2\cos\theta_j dr_j d\theta_j-\int_0^{2\pi}\int_{-h_j}^{0}\varphi_{RD-E}^{j}\,|_{r=a_j}\,(z-\overline{z}_j)\,a_j\cos\theta_j d\theta_j dz\right) \\
&= \mathrm{i}\omega_0\rho\left[\int_0^{2\pi}\int_0^{a_j}\mathrm{i}\omega_0\sum_{s=1}^{5}\left(\zeta_s^{(j)}\varphi_{RD-Cs}^{(jj)}+\sum_{k=1,\mathrm{k}\neq j}^{N}\zeta_s^{(k)}\varphi_{RD-Cs}^{(jk)}\right)\Bigg|_{z=-h_j} r_j{}^2\cos\theta_j dr_j d\theta_j\right. \\
&\quad\left.+\int_0^{2\pi}\int_{-h_j}^{0}\mathrm{i}\omega_0\sum_{s=1}^{5}\left(\zeta_s^{(j)}\varphi_{RD-Es}^{(jj)}+\sum_{k=1,\mathrm{k}\neq j}^{N}\zeta_s^{(k)}\varphi_{RD-Es}^{(jk)}\right)\Bigg|_{r=a_j}(z-\overline{z}_j)\,a_j\cos\theta_j d\theta_j dz\right] \\
&= \sum_{s=1}^{5}\left[\zeta_s^{(j)}\left(-\omega_0{}^2\rho\int_0^{2\pi}\int_0^{a_j}\varphi_{RD-Cs}^{(jj)}\Big|_{z=-h_j} r_j{}^2\cos\theta_j dr_j d\theta_j-\omega_0{}^2\rho\int_0^{2\pi}\int_{-h_j}^{0}\varphi_{RD-Es}^{(jj)}\Big|_{r=a_j}(z-\overline{z}_j)\,a_j\cos\theta_j d\theta_j dz\right)\right. \\
&\quad\left.+\sum_{k=1,k\neq j}^{N}\zeta_s^{(k)}\left(-\omega_0{}^2\rho\int_0^{2\pi}\int_0^{a_j}\varphi_{RD-Cs}^{(jk)}\Big|_{z=-h_j} r_j{}^2\cos\theta_j dr_j d\theta_j-\omega_0{}^2\rho\int_0^{2\pi}\int_{-h_j}^{0}\varphi_{RD-Es}^{(jk)}\Big|_{r=a_j}(z-\overline{z}_j)\,a_j\cos\theta_j d\theta_j dz\right)\right] \\
&= \sum_{s=1}^{5}\left(\zeta_s^{(j)}F_{RD5s}^{(jj)}+\sum_{k=1,k\neq j}^{N}\zeta_s^{(k)}F_{RD5s}^{(jk)}\right)=\sum_{s=1}^{5}\sum_{i=1}^{N}F_{RD5s}^{(ji)}\zeta_s^{i},
\end{aligned} \tag{43}$$

where $\overline{z}_j$ is the vertical coordinate of the center of mass of cylinder j.

$\mathcal{F}_{IDp}^{(j)}$ is the exciting force/moment on cylinder j in the presence of ambient incident waves, independent of oscillations of cylinders; $\mathcal{F}_{RDp}^{(j)}$ $(= \sum_{s=1}^{5}\sum_{i=1}^{N} F_{RDps}^{(ji)}\zeta_s^{(i)})$ is the hydrodynamic force/moment on cylinder j induced by oscillations of cylinders in the absence of ambient incident waves, which is directly proportional to the amplitudes of oscillations. $F_{RDps}^{(ji)}\zeta_s^{(i)}$ is the pth-direction hydrodynamic force/moment on the jth cylinder due to the sth-direction oscillation of the ith cylinder with amplitude $\zeta_s^{(i)}$.

As a result, the equation of motion for cylinder j in the pth direction is obtained, as shown below

$$\left(-\omega^2 M_p^{(j)} - \mathrm{i}\omega\lambda_p^{(j)} + \delta_p^{(j)} + k_p^{(j)}\right)\zeta_p^{(j)} - \sum_{s=1}^{5}\sum_{i=1}^{N} F_{RDps}^{(ji)}\zeta_s^{(i)} = \mathcal{F}_{IDp}^{(j)}, \quad j = 1, 2, \ldots, N; \quad p = 1, 2, \ldots, 5, \tag{44}$$

where $M_p^{(j)}$ denotes the mass ($p = 1, 2, 3$) or moment of inertia ($p = 4, 5$) of cylinder j. λ_p^j and δ_p^j denote the mechanical damping and stiffness of cylinder j in direction p respectively, caused by the power take-off and mooring systems. $k_p^{(j)}$ denotes the hydrostatic restoring stiffness of cylinder j in direction p. Finally, by solving linear equations of Eq. (44), the amplitude $\zeta_p^{(j)}$ of each floating cylinder in each direction can be obtained, thereby solving the whole problem completely. As an additional result, the added mass and damping coefficients can also be straightforwardly obtained as well:

$$\begin{aligned} a_{ps}^{(ji)} &= \mathrm{Re}\left[F_{RDps}^{(ji)}\right]/\omega^2 \\ b_{ps}^{(ji)} &= \mathrm{Im}\left[F_{RDps}^{(ji)}\right]/\omega \end{aligned} \tag{45}$$

3. Results and discussions

3.1. Verification

In Section 2 of this paper, a semi-analytical method for the hydrodynamic responses of truncated cylinders in an array with relative motions in the presence of ambient incident waves is proposed. This method can solve the problem that each cylinder is allowed to oscillate with five DOFs of translation and rotation, and the amplitudes of each cylinder in the array can be different. This section verifies the method. At present, there are hardly any published results on such an array in which each cylinder oscillates with five DOFs. The results of some published examples can be regarded as the degradation cases. Hence, these examples were recalculated by the method in Section 2 and compared with existing results.

Matsui and Tamaki (1981) used the boundary element method to calculate the oscillation amplitudes of two DOFs (surge and heave) for an array with relative motions consisting of two truncated cylinders in the presence of incident waves. The two cylinders are distributed along the X direction, with the spacing between the two cylinders being $3a$. Each cylinder has a radius of a, a draught of $0.5a$, and a moment of inertia of $0.75\rho a^5$. The heading angle of the ambient incident wave is $\beta = 0$ and the water depth is $10a$. The comparison between the results of the present study and those of Matsui and Tamaki (1981) is shown in Fig. 2(a, b), they are in good agreement. Wang et al. (2004) calculated the variations in the pitch amplitude of the two above cylinders with wave frequencies using the numerical method of the free-surface Green function source distribution. The results of the present study are also in good agreement with those of Wang et al. (2004), as shown in Fig. 2(c). Zhong and Yeung (2019) used a semi-analytical method to calculate the surface-wave interactions among an array of truncated cylinders. They calculated the exciting forces and damping coefficients of the four cylinders moving as a whole. The cylinders are arranged as shown in Fig. 5. Each cylinder has a radius of a and a draught of $2a$, with the spacing between the two cylinders being $8a$ and the water depth being $10a$. As before, the results of our study are in good agreement with those of Zhong and Yeung (2019), as shown in Fig. 3.

In addition, many published results on the cylinder array's added mass and damping coefficient of cylinder array exist. The author of this paper has previously made many comparisons (e.g., Zeng et al., 2016). Another example comparison is given in this section. Mavrakos (1991) used the multiple scattering method to calculate the coupling hydrodynamic coefficients of three cylinders arranged in an equilateral triangle. The results of the present study are in good agreement with his results, as shown in Fig. 4.

3.2. Upper bounds of summation and computation time

Upper bounds of summation

In existing studies on diffraction and radiation of water waves, there have been some works on the upper bounds of summation (i.e. the number of terms retained in the eigenfunction expansion) required for convergence. For the diffraction and radiation problems of truncated cylinder groups, Kagemoto and Yue (1986) showed that good convergence results can be achieved when the upper bound of summation M is taken as 2 and N_m is taken as 4 (using the symbols in this paper, that is, $m_0 = 4$, $n_0 = 2$). For radiation problem of arrays of independently oscillating truncated cylinders, Zeng et al. (2016) showed that good convergence results can be obtained when $m_0 = 6$, $n_0 = 25$ for the cases they studied.

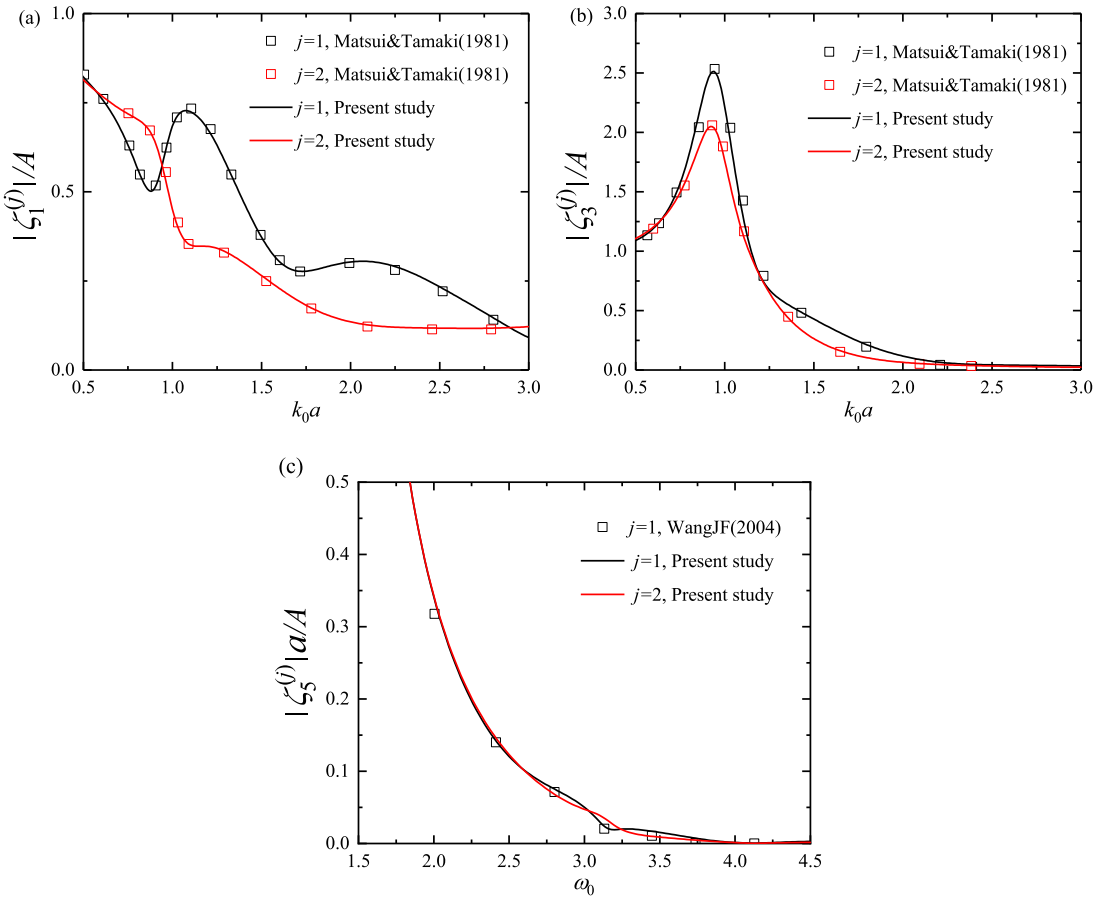

Fig. 2. Surge (a), heave (b) and pitch (c) amplitudes of the two cylinders.

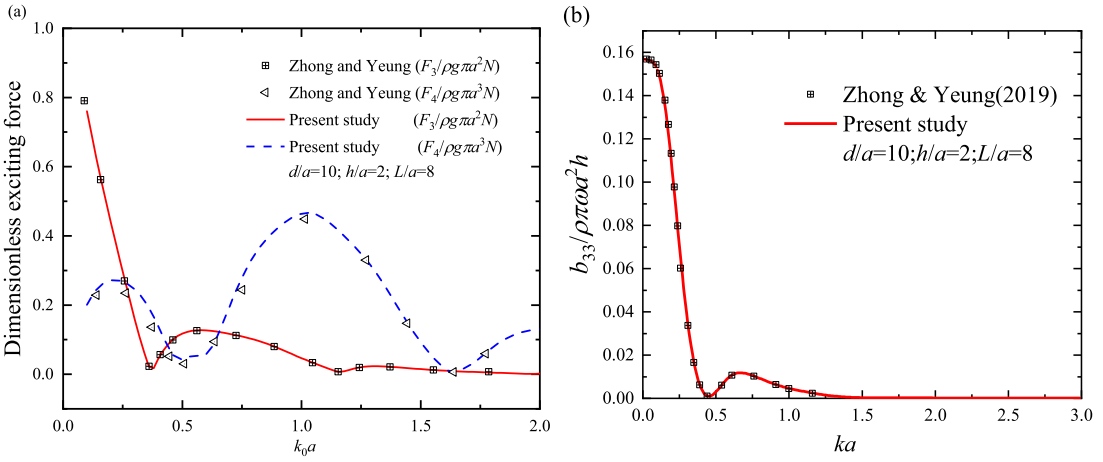

Fig. 3. Exciting forces and damping coefficient of the four cylinders.

For the problems related to the motion of a cylinder array in the presence of incident waves, there are hardly any published results on the influence of the upper bounds of the summation on the convergence. This study investigated this problem in the computation process. According to our computations on the motions of arrays of independently oscillating truncated cylinders with five DOFs in the presence of incident waves, the smaller the ratio of the draught to water depth is, the more terms for convergence are required. This finding is similar to the result of Zeng et al. (2016)

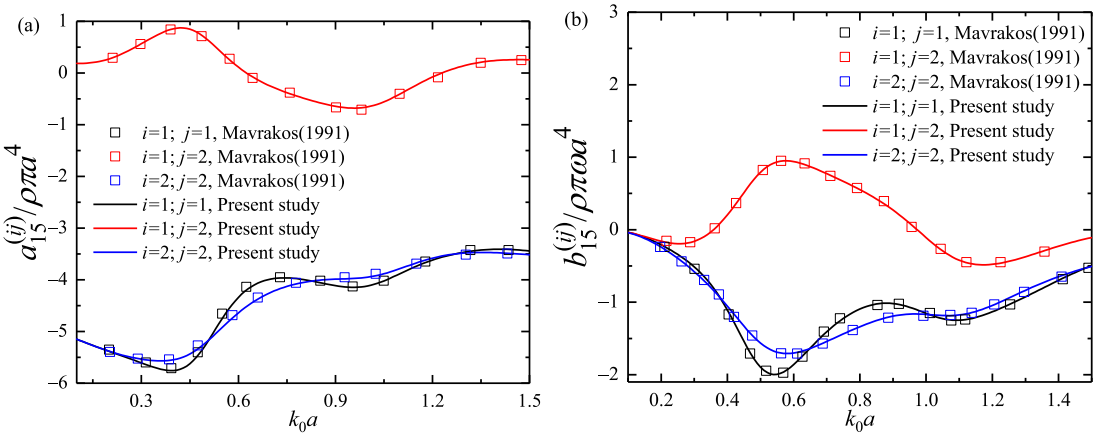

Fig. 4. Hydrodynamic coefficients of the three cylinders. (a): the added mass; (b): the damping coefficient.

on the upper bounds of summation in the radiation problem. For the cases we investigated, our computations also show that convergence results are obtained for all considered wavenumbers when m_0 is taken as 5 and n_0 as 25.

We evaluate the convergence behaviors by comparing the results obtained when the upper bounds of summation are small with those when the upper bounds of summation are large enough. Investigations revealed that when m_0>5, even if we continue to increase the upper bound of summation m_0, there is no significant change in the calculation results (the error is less than 0.1%). Moreover, increasing m_0 will greatly increase the calculation time. So, taking m_0 as 5 is enough. Corresponding tests were also conducted for n_0. It was found that when n_0>25, even at the cost of significantly increasing the calculation time, increasing n_0 does not significantly change the calculation results (the error is within 1%). Therefore, it is sufficient to take n_0 as 25.

Computation time

The computation time in this study depends on the upper bounds of summation (m_0 and n_0) and the number of cylinders (N). For the configuration with four truncated cylinders, the computation time for one wave number is about 145.8 s, and the error is less than 1% when $m_0 = 5$ and $n_0 = 25$ are selected. If the accuracy requirements are relaxed, e.g. the error is kept within 5%, the computation time is about 77.6 s. The computer system used is Intel(R) Xeon(R) W-2133 CPU @ 3.60 GHz with 6 cores and 12 threads, and the RAM is 32.0 GB.

Our computations show that for other cases with different numbers of cylinders, selecting $m_0 = 5$ and $n_0 = 25$ can still give results with good accuracy (when the error is about 1%). Therefore, we propose that $m_0 = 5$ and $n_0 = 25$ can be generally selected for computation. Even if m_0 and n_0 are fixed, the computation time depends on many factors, such as the number of cylinders, the efficiency of matrix generation, the efficiency of solving linear equations, the performance of the computer, and so on, making it difficult to express this dependency accurately with explicit expressions. Our computations show that, by and large, with an increase in the number of cylinders, the computation time roughly shows a piecewise linear growth with different slopes. Its growth rate is faster than the linear growth and slower than the square law growth.

3.3. The responses of an array with relative motions composed of four truncated cylinders in the presence of ambient incident waves

In this section, the dynamic responses of an array with relative motions consisting of four truncated cylinders in the presence of ambient incident waves are calculated using the method developed in Section 2. As shown in Fig. 5, each cylinder is of radius a, draught $0.5a$, and moment of inertia $0.75\rho\pi a^5$. The spacing between the two cylinders is L. The heading angle of the ambient incident wave is β. Each cylinder in the array is allowed to experience oscillations of five DOFs (surge, sway, heave, roll, and pitch) with different amplitudes. Since there have been many studies on the wave excitation forces and the hydrodynamic coefficients for arrays of cylinders in academic publications, this section mainly focuses on the amplitudes of each cylinder and free surface elevation in the presence of incident waves. At present, there are few concrete computations of the oscillation amplitude of the cylinder array. A tiny number of results based on the discrete numerical method are that each cylinder oscillates with only two degrees of freedom. There are hardly any specific results for the case that each cylinder experiences five DOFs oscillations with different amplitudes. Therefore, in this section, we perform computations for this problem and investigate the effects of cylinder spacing L and wave incidence angle β on the oscillation amplitude.

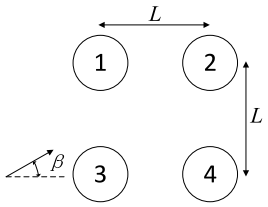

Fig. 5. The configuration for an array composed of four cylinders.

Amplitudes of each cylinder with five degrees of freedom at different wave incidence angles

Fig. 6 shows the amplitude responses of the array with relative motions in the presence of incident waves at five different incidence angles for $L = 4a$. The red, blue, green, pink and brown lines represent the results for $\beta = 0$, $\beta = \pi/8$, $\beta = \pi/4$, $\beta = 3\pi/8$ and $\beta = \pi/2$, respectively. Variations in the surge, sway, heave, roll and pitch amplitudes of cylinders 1 and 4 with dimensionless wavenumber k_0a are plotted. The black line indicates the amplitudes of an isolated cylinder with $\beta = 0$.

It is evident that when $\beta = 0$, the isolated cylinder's sway and roll amplitudes are zero. However, as shown in Fig. 6(c), (d), (g), and (h), for a cylinder in the array, the sway and roll amplitudes are usually not zero due to the hydrodynamic interactions among cylinders.

Since the array shown in Fig. 5 is a square layout, the amplitudes of each cylinder should have some symmetry. This is also confirmed by the computation results shown in Fig. 6, which shows that the surge (sway) amplitude of cylinder 1 at incidence angle β is equal to the sway (surge) amplitude of cylinder 4 at incidence angle $\pi/2$ - β, the heave amplitude of cylinder 1 at incidence angle β is equal to the heave amplitude of cylinder 4 at incidence angle $\pi/2$ - β, and the pitch (roll) amplitude of cylinder 1 at incidence angle β is equal to the roll (pitch) amplitude of cylinder 4 at incidence angle $\pi/2$ - β. These results are in line with expectations, indicating this study's accuracy.

The heave of a single isolated cylinder is not coupled with other DOFs. For the isolated cylinder in this example, the variation curve of heave amplitude with k_0a has a resonant peak at $k_0a = 0.99$, as shown in the black line in Fig. 6(e) and (f). The situation is different for the cylinder-array. Since the four cylinders are coupled together through hydrodynamic interactions, the motion equations for the four-cylinder-array are coupled equations with 20 DOFs. The peak position of each cylinder's heave amplitude curve is different from that of the isolated cylinder, as shown in other color curves in Fig. 6(e) and (f). The difference between the amplitude peak positions of cylinders in the array and an isolated cylinder reflects the influence of hydrodynamic interactions among cylinders.

For cases with different wave incidence angles, the variations in the amplitude with k_0a are complex. When the wavelength of the incident wave is long (k_0a < 0.7 in this example), the variation trend of each cylinder's amplitude with k_0a is close to that of an isolated cylinder. In this region, with an increase in the wave incidence angle, the surge/pitch decreases, and the sway/roll increases. It is also observed that each cylinder's DOF amplitude in the array has a peak near $k_0a \sim 1$. This is because the region $k_0a \sim 1$ is where the heave resonance peak is located. Therefore, not only the heave of each cylinder has the maximum value in this region, but also the amplitudes of other DOFs have local extreme points in this region due to the hydrodynamic interactions among each DOF. The heave of an isolated cylinder is not coupled with other DOF, so for an isolated cylinder, the amplitudes of other DOFs are not affected by the heave peak.

When the incidence angle is $\beta = \pi/2$ (or $\beta = 0$), the hydrodynamic force on each cylinder induced by the incident wave velocity potential (the Froude–Krylov force) does not contribute to the surge and pitch (sway and roll) of each cylinder. At this time, the surge and pitch (sway and roll) are completely caused by the radiation and diffraction hydrodynamic interactions among the cylinders. Therefore, the variation trends of surge and pitch (sway and roll) differed from those of the cases with other incidence angles but are similar to that of the heave amplitude curve for $\beta = \pi/2$ (or $\beta = 0$), having obvious peaks near $k_0a \sim 1$.

Amplitudes of each cylinder with five degrees of freedom for different cylinder spacings

Fig. 7 shows the amplitude responses of the array for cases with three different cylinder spacing in the presence of incident waves with $\beta = 0$. The red, blue, and green lines represent the results for $L = 4a$, $L = 6a$ and L = $10a$, respectively. Variations in the surge, sway, heave, roll and pitch amplitudes of cylinders 1 and 4 with dimensionless wavenumber k_0a are plotted. Cylinders 1 and 4 represent the situations of the upstream and downstream cylinders respectively. The black line indicates the amplitude of an isolated cylinder, which can also be regarded as the case of infinite cylinder spacing.

As shown in Fig. 7(a), while variations in the surge amplitude of an isolated cylinder with wavenumbers show a monotonically decreasing curve, the situation differs for cylinders in the array. Due to the hydrodynamic interactions among the cylinders, although the surge amplitude of cylinder 1 does not decrease monotonically with the increase of wavenumber, it fluctuates around the amplitude response curves of an isolated cylinder. Also, with an increase in cylinder spacing L, this fluctuation becomes more rapid. Previously, Zeng et al. (2019) conducted a detailed study on the fluctuation phenomenon of excitation forces for a long array of bottom-mounted cylinders. Then they revealed the mechanism of the

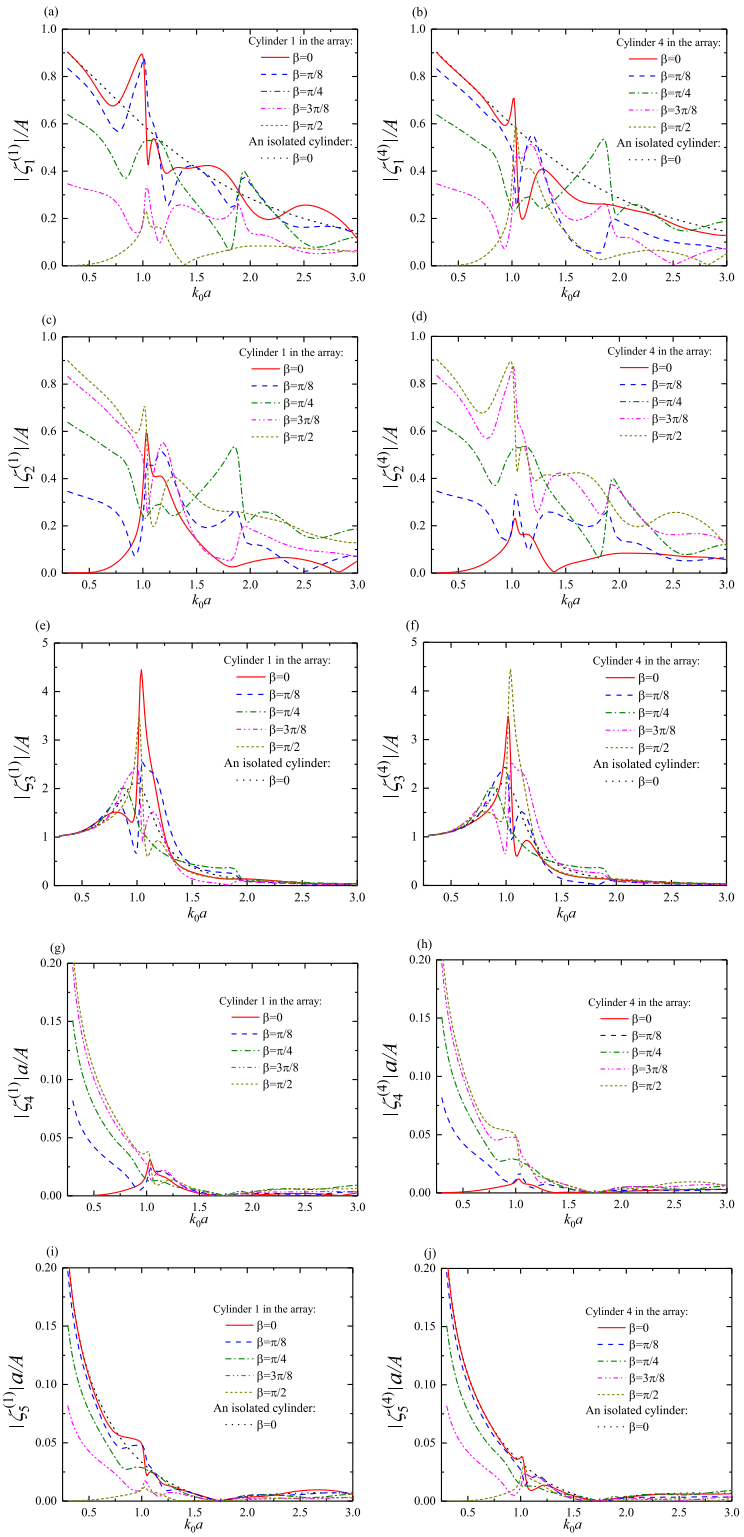

Fig. 6. Amplitude responses of cylinder 1 (a, c, e, g, i) and cylinder 4 (b, d, f, h, j) at five incident wave angles (L = 4a). (For interpretation of the references to color in this figure legend, the reader is referred to the web version of this article.)

amplitude fluctuation of the wave excitation force. This work, however, studies the situation of an array of cylinders allowed to oscillate, which is more complex than that of a bottom-mounted cylinder array. Nevertheless, the fluctuation phenomenon in Fig. 7(a) can still be understood by referring to the analysis of Zeng et al. (2019): The amplitude fluctuation is caused by the constructive and destructive interference of the diffraction and radiation waves emitted from the cylinders at the upstream and downstream ends of the array, and the fluctuation period decreases with an increase in the cylinder spacing. The peak near $k_0a \sim 1.0$ in Fig. 7(a) is caused by resonance in the heave-dominated mode of the cylinder array.

Similarly, the curves in Fig. 7(b) – (j) also have such fluctuations and peaks. For the case of $L = 4a$, the heave peaks of cylinders in the four-cylinder-array appear at $k_0a = 1.04$, while the resonant peak of the heave of an isolated cylinder is at $k_0a = 0.99$, which indicates a natural frequency of four-cylinder-array that is close to the heave's natural frequency of an isolated cylinder. At the natural frequency of the heave-dominated mode of the cylinder array ($k_0a = 1.04$), the peaks of sway and roll are also obvious, while the peaks of surge and pitch are less obvious. This is because Fig. 7 is obtained when the incidence angle is $\beta = 0$. At this time, the velocity potential of the incident wave does not contribute to swaying/rolling excitation forces/moments, and the sway and roll amplitude are completely generated by the diffraction and radiation potentials of the array. The radiation potential also has peaks at the frequency corresponding to the heave peak, resulting in sway and roll amplitudes peaks. With changes in cylinder spacing, the natural frequencies of the array system change, and the peak positions of motion amplitudes of cylinders in the array also change consequently.

We note that several large peaks at heave resonance in Figs. 6 and 7 indicate that the linear water wave theory is not strictly valid when the resonance amplitude is large. The linear water wave theory is valid in the wide range of non resonant regions in which motions are small. Although the motion amplitude obtained in the resonant region is not very accurate using a linear theory, it can fairly accurately give an effective estimate of the natural frequency of the array system consisting of independently oscillating cylinders. In order to obtain an accurate value for the motion amplitudes of every cylinder in the array at resonance, the nonlinear wave theory (even the viscosity should also be considered) should be used. It is expected that the values of motion amplitudes obtained by the higher-order theory in the case of resonance will be smaller than that of linear wave theory, but the frequency corresponding to the peak will not differ greatly from the frequency obtained by the linear theory.

Elevation of free surface

Subsequently, we investigate the free surface elevation amplitude, η/A, for the array of relative motions consisting of four cylinders in the presence of incident waves. The results for the cases with incidence angle $\beta = 0$, cylinder spacing $L = 4a$, and wavenumber k_0a being 0.5, 1.0, 1.5 and 2.0 are presented. While the left column of Fig. 8 (i.e. Fig. 8(a), (c), (e), and (g)) shows the amplitude of free surface elevation for the array with relative motions, the right column (i.e. Fig. 8(b), (d), (f), and (h)) shows that of the corresponding fixed array for comparison.

As shown in Fig. 8(a) and (b), the amplitude of the free surface elevation is relatively small in the case of $k_0a = 0.5$. When the array is allowed to oscillate under the action of waves, while the free surface amplitude in the inner area of the array is smaller than that when the array is fixed, the free surface amplitude in the downstream area of the array is larger than that in the fixed case.

However, in the case of $k_0a = 1.0$, as shown in Fig. 8(c), the maximum free surface amplitude appears in the area surrounded by cylinders for the array with relative motions, with the maximum reaching 2.52. When the array is fixed, as shown in Fig. 8(d), the maximum free surface amplitude appears in the area between cylinders 1 and 3, and the maximum is 2.37, less than the array with relative motions. The free surface amplitude in the downstream area of array with relative motions is also larger than that of the fixed array.

Then, in the case of $k_0a = 1.5$, as shown in Fig. 8(e), for array with relative motions, the maximum free surface amplitude appears in the area between cylinders 1 and 3 with a value of 2.07. For a fixed array, as shown in Fig. 8(f), the maximum free surface amplitude of 1.87 appears in immediate areas at the front of cylinders 1 and 3. Different from the first two cases, at this wavenumber, the free surface amplitude downstream the array with relative motions is less than that downstream the fixed array.

Finally, in the case of $k_0a = 2.0$, as shown in Fig. 8(g) and (h), the distribution of the free surface amplitude of the array with relative motions is very close to that of the fixed array.

It is evident from Fig. 8 that the free surface amplitude distribution of the array with relative motions becomes closer to that of the fixed array with an increase in the wavenumber. This is because the larger the wavenumber, the more the wave force frequency is greater than the natural frequency of the array system, so that the response of the array system will be closer to that of the fixed array.

4. The influence of the factor that each cylinder in the array is allowed to oscillate with five degrees of freedom on the WEC array's performance

For the WEC array composed of multiple oscillating buoys, existing studies usually model each buoy as a truncated cylinder with a single DOF (heave) for hydrodynamic analysis. This section considers two models that each cylinder is allowed to oscillate with five DOFs and only a single DOF (heave). By comparing the results of the two models, the influence of each cylinder's five DOFs oscillations on the wave energy extraction performance of the WEC array is revealed.

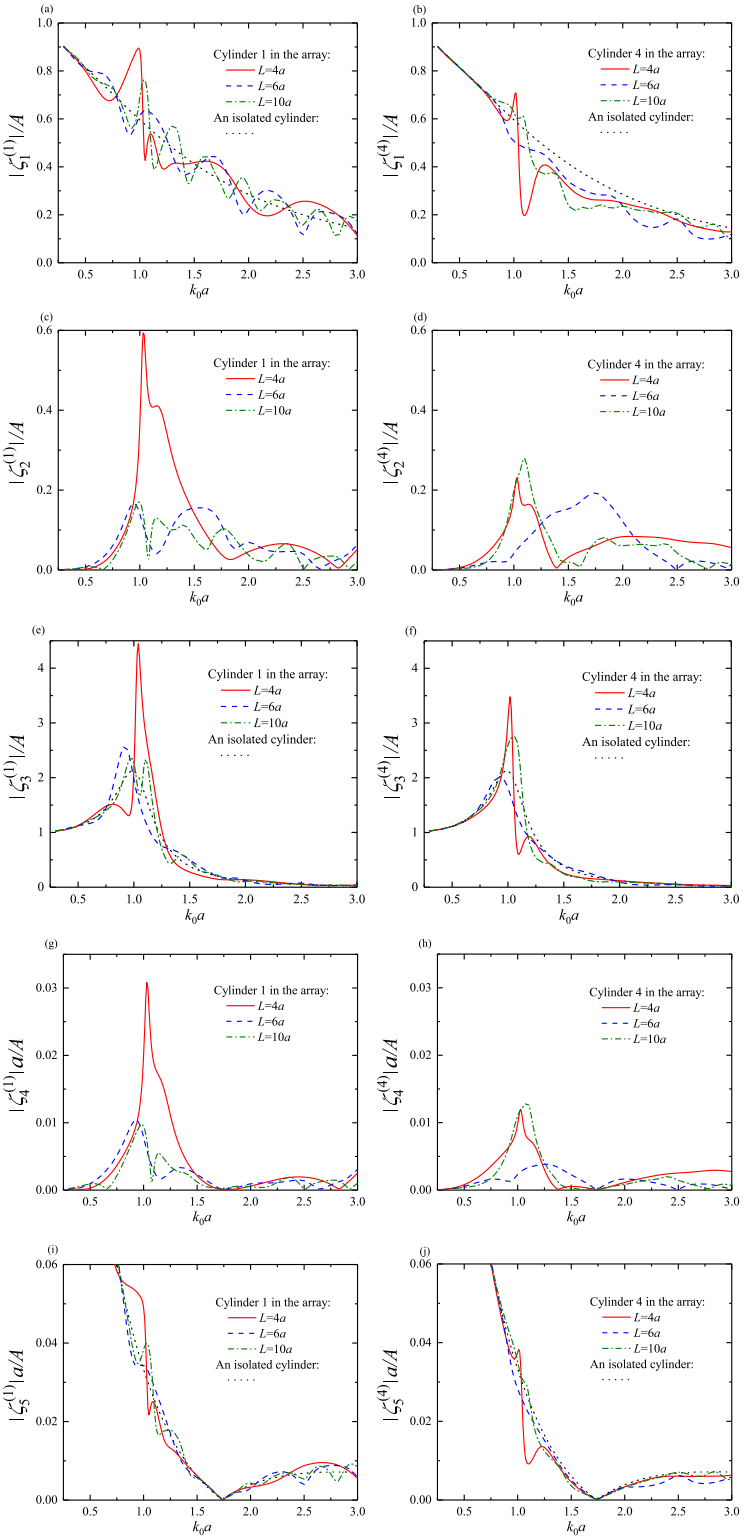

Fig. 7. Amplitudes of cylinders 1 (a, c, e, g, i) and 4 (b, d, f, h, j) for different cylinder spacings *L*. (For interpretation of the references to color in this figure legend, the reader is referred to the web version of this article.)

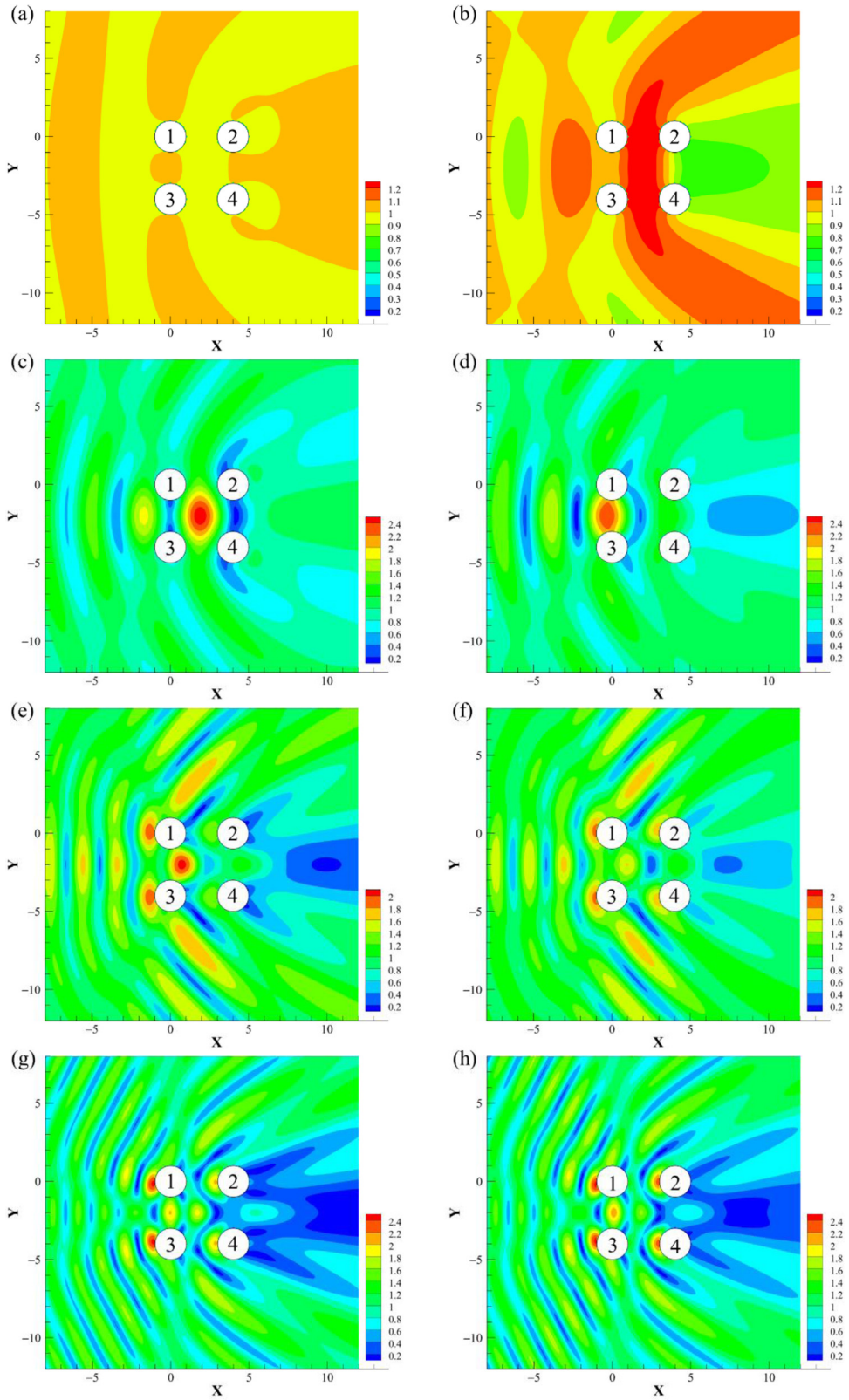

Fig. 8. Free surface amplitudes (η/A) of arrays with relative motions (a, c, e and g) and fixed arrays (b, d, f and h) at different wave numbers. (a) and (b): k_0a = 0.5; (c) and (d): k_0a = 1.0; (e) and (f): k_0a = 1.5; (g) and (h): k_0a = 2.0.

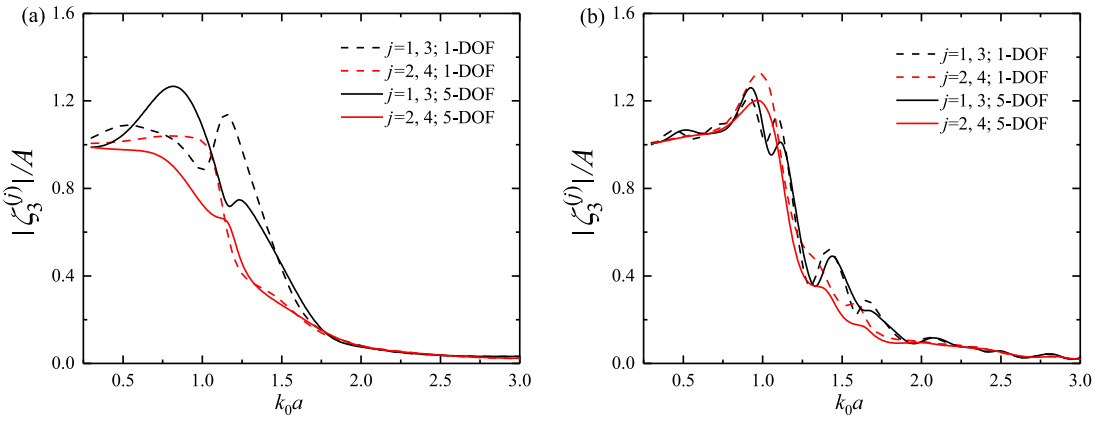

Fig. 9. Amplitude responses of a WEC array based on the 1-DOF model (Model 1) and the 5-DOF model (Model 2). (a): L = 3a; (b): L = 10a.

The two models are named Model 1 and Model 2 respectively. While Model 1 is a single DOF model (i.e. 1-DOF model), Model 2 is a five DOFs model (i.e. 5-DOF model). In Model 1, each cylinder has only one DOF of heave, and the power take-off characteristics of each cylinder are considered linear and set to δ (stiffness) and λ (damping). In Model 2, however, each cylinder has five DOFs comprising the surge, sway, heave, roll, and pitch, with the power take-off characteristics in the heave direction set to the same parameters as that of Model 1, and the mechanical stiffness and damping in other directions set to 0 (i.e. no power is extracted in other directions).

According to Falnes (2002), the mean power extracted by cylinder j oscillating in the heave direction with amplitude $\zeta_s^{(j)}$ should be

$$P_s^j = \frac{1}{2}\omega^2\lambda_s\left|\zeta_s^{(j)}\right|^2. \tag{46}$$

There are two important indicators describing the performance of a WEC array: the capture width w and interaction factor q, as shown in Eqs. (47) and (48), which are used to represent the total wave power extraction capacity of the array and determine whether the hydrodynamic interactions among cylinders in the array are conducive to wave power generation.

$$w = \frac{\sum_{i=1}^{N}\sum_{s=1}^{5}P_s^{(i)}}{P_l}, \tag{47}$$

$$q = \frac{\sum_{i=1}^{N}\sum_{s=1}^{5}P_s^{(i)}}{N\times\sum_{s=1}^{5}P_s^{iso}}, \tag{48}$$

where P_l denotes the power flux of the ambient incident wave, as shown below

$$P_l = \frac{1}{2}\rho g A^2\cdot\frac{\omega_0}{2k_0}\left(1+\frac{2k_0d}{\sin h2k_0d}\right). \tag{49}$$

Subsequently, the computation is performed for a WEC array composed of four truncated cylinders, whose sizes have been described in Section 3.2, with two different cylinder spacings being considered. Let $\delta = 0$ and $\lambda = 0.44\rho a^3\omega_n$, where the value of λ equals the radiation damping of an isolated cylinder at heaving resonance frequency ω_n. Fig. 9 shows the comparison results of the heave amplitude of each cylinder in the WEC array based on Model 1 and Model 2. The results of arrays with small and large cylinder spacings are shown in Fig. 9(a) ($L = 3a$) and Fig. 9(b) ($L = 10a$), respectively. Since the wave incidence angle $\beta = 0$, the amplitude responses of cylinders 1 and 3 are identical, the same is true for cylinders 2 and 4. It is evident from Fig. 9 that the heave amplitude of the same cylinder in the array is quite different using the 1-DOF and the 5-DOF models. As shown in Fig. 9(a), at $k_0a = 1.16$, the dimensionless amplitudes of cylinders 1 and 3 (Upstream cylinders of the array) reach 1.14 based on the 1-DOF model while it is 0.72 based on the 5-DOF model that if the 1-DOF model is used to analyze the problem which is actually a 5-DOF problem, the error is as high as 57%. The difference between the results of the two models for downstream cylinders of the array (cylinder 2 or 4) is also large at $k_0a = 1.0$, which is 39%. This difference still exists when the cylinder spacing changes. For example, as shown in Fig. 9(b), the error is 22% for the upstream cylinder at $k_0a = 1.66$, and 37% for the downstream cylinder at $k_0a = 1.30$.

It can be seen from Eqs. (46), (47), and (49) that the result of the oscillating amplitudes of each cylinder will directly affect the wave power extraction performance of the array. Fig. 10 shows the comparisons of the capture width w of a WEC array based on the two different models. As shown in Fig. 10(a), the 1-DOF model underestimates the capture width when $0.65 < k_0a < 0.97$, while it overestimates the capture width when $0.97 < k_0a < 1.49$. The difference between the two models reaches 71% at $k_0a = 1.13$. As shown in Fig. 10(b), when the cylinder spacing is large ($L = 10a$), the 1-DOF model overestimates the capture width at almost all wavenumbers, and the biggest difference reaches 51% at $k_0a = 1.33$.

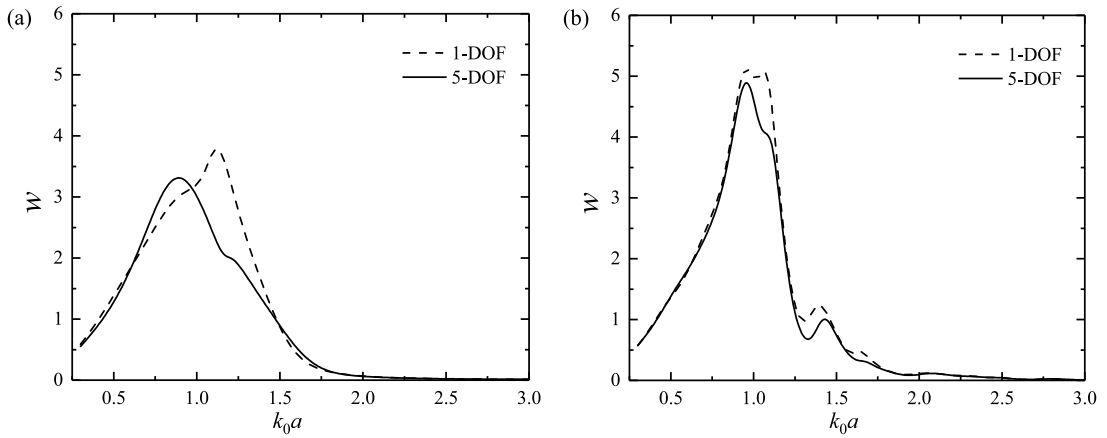

Fig. 10. Capture width w of a WEC array based on the 1-DOF and 5-DOF models. (a) L = 3a and (b) L = 10a.

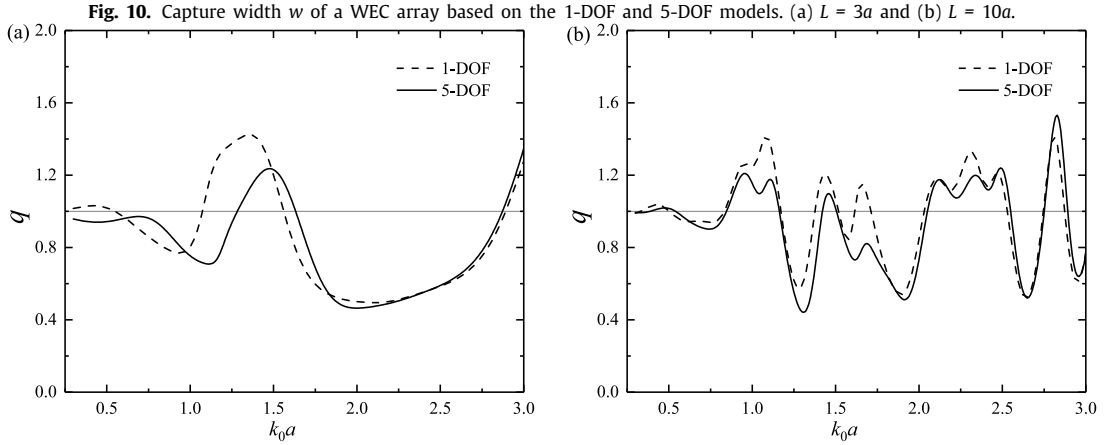

Fig. 11. Interaction factor q of a WEC array with the 1-DOF and 5-DOF models. (a) L = 3a and (b) L = 10a.

Fig. 11 shows the comparisons of the interaction factor q of a WEC array based on the two different models. $q > 1$ means that the power extraction performance of the WEC array is better than that of the same number of isolated WECs, which indicates that the hydrodynamic interactions among cylinders are constructive to the array performance. $q < 1$ means that the interactions are destructive. As shown in Fig. 11(a), at $k_0a = 1.17$, the q factor reaches 1.30 based on the 1-DOF model, while it is only 0.75 based on the 5-DOF model, the difference is up to 73% for the case L=3a. As shown in Fig. 11(b), the biggest difference reaches 45% at $k_0a = 1.66$ for the case $L = 10a$.

It can be seen that if the other degrees of freedom are not fully constrained, even if only the oscillation in the heave direction is used to generate power, it is recommended to consider the effect of other degrees of freedom on hydrodynamic modeling and analysis; otherwise, it may lead to large errors.

Incidentally, for WEC arrays with large individual energy absorption but small q coefficient, it may be possible to consider how to further improve its interaction coefficient through layout optimization, and to improve the capture width as well. It is also recommended to use the 5-DOF hydrodynamic model for layout optimization.

5. Extensions to the situation of irregular waves

In the previous sections, we studied the hydrodynamic interactions between single-directional harmonic waves and arrays of cylinders. However, this section will discuss the situation when incident waves are omnidirectional irregular waves.

To analyze the hydrodynamic interactions between waves and arrays of floating cylinders in the presence of multidirectional irregular incident waves, a multidirectional irregular model presented in Yu et al. (1991) is adopted to represent the incident waves, in which the omnidirectional irregular waves are expressed by the superposition of many regular component waves. As a result, the free surface elevation $\eta_I(X, Y, t)$ of incident waves at point (X, Y) can be expressed, as shown below

$$\eta_I(X,Y,t) = \mathrm{Re}\left\{\sum_{\mu=1}^{M}\sum_{\nu=1}^{N} a_{\mu\nu} e^{-i[\omega_{\mu\nu}t - k_{\mu\nu}(X\cos\theta_\nu + Y\sin\theta_\nu) - \varepsilon_{\mu\nu}]}\right\} \tag{50}$$

where

$$\omega_{\mu\nu} = \overline{\omega}_\mu - \frac{\delta\omega}{2} + (\nu - 1 + r_{\mu\nu})\frac{\delta\omega}{N} \tag{51}$$

$$a_{\mu\nu} = \sqrt{2S(\overline{\omega}_\mu, \theta_\nu)\delta\omega\,\delta\theta} \tag{52}$$

$\varepsilon_{\mu\nu}$ is the random phase with a uniform distribution from 0 to 2π, and $r_{\mu\nu}$ is a random number uniformly distributed within the interval [0, 1], introduced to impart a random component to $\omega_{\mu\nu}$. $a_{\mu\nu}$, $\omega_{\mu\nu}$, and $k_{\mu\nu}$ are the amplitude, angular frequency, and wavenumber of the component wave, respectively.

$$\overline{\omega}_\mu = \frac{1}{2}(\omega_\mu + \omega_{\mu-1}) \tag{53}$$

$$\omega_\mu = \omega_H - \mu \cdot \delta\omega \tag{54}$$

$$\delta\omega = \frac{\omega_H - \omega_L}{M} \tag{55}$$

$$\delta\theta = \frac{\theta_{\max} - \theta_{\min}}{N} \tag{56}$$

where ω_L and ω_H are the minimum and maximum angular frequencies, respectively. The interval $[\omega_L, \omega_H]$ is equally divided into M parts. θ_ν is the incident angle of the component wave. The interval $[\theta_{\min}, \theta_{\max}]$ is equally divided into N parts. $[\theta_{\min}, \theta_{\max}]$ is the direction distribution interval, which is $[-\pi/2, \pi/2]$.

Generally, the directional spectrum $S(f, \theta)$ can be considered as the product of a frequency spectrum $S(f)$ and a directional spreading function $G(f, \theta)$, i.e.,

$$S(f, \theta) = S(f)G(f, \theta) \tag{57}$$

JONSWAP spectrum recommended by Goda (1999) is used for the frequency spectrum in this study.

$$S(f) = \beta_J H_{1/3}^2 T_p^{-4} f^{-5} \exp\left[-1.25(T_p f)^{-4}\right] \cdot \gamma^{\exp\left[-(T_p f - 1)^2/2\sigma^2\right]} \tag{58}$$

where

$$\beta_J = \frac{0.06238}{0.230 + 0.0336\gamma - 0.185(1.9 + \gamma)^{-1}} \times [1.094 - 0.01915 \ln \gamma] \tag{59}$$

$$T_p = \frac{T_{1/3}}{1.0 - 0.132(\gamma + 0.2)^{-0.559}} \tag{60}$$

$$\sigma = \begin{cases} 0.07 & f \le f_p \\ 0.09 & f > f_p \end{cases} \tag{61}$$

$H_{1/3}$, $T_{1/3}$, T_p, f_p are the significant wave height, the significant period, the peak period, and the peak frequency, respectively, and γ is the peak enhancement factor, which takes a value of 3.3 in this study.

For multidirectional irregular waves, the total energy should equal that of unidirectional irregular waves. This means that the spectrum and directional spectrum need to satisfy the following relationship

$$\int_0^\infty S(f)df = \int_0^\infty \int_{\theta_{\min}}^{\theta_{\max}} S(f, \theta)\mathrm{d}\theta\, df \tag{62}$$

Then the direction spreading function $G(f, \theta)$ must satisfy

$$\int_{\theta_{\min}}^{\theta_{\max}} G(f, \theta)d\theta = 1 \tag{63}$$

The Mitsuyasu-type spreading function is adopted here for the directional spreading function, defined by Longuet-Higgins et al. (1963) as

$$G(f, \theta) = G_0(\tau)\cos^{2\tau}\left(\frac{\theta - \theta_0}{2}\right) \tag{64}$$

where τ is the directional spreading parameter (the larger the parameter τ, the narrower the direction distribution) and θ_0 is the principal wave direction. By combining (63) and (64), $G_0(s)$ can be solved as follows:

$$G_0(\tau) = \left[\int_{\theta_{\min}}^{\theta_{\max}} \cos^{2\tau}\left(\frac{\theta - \theta_0}{2}\right) d\theta\right]^{-1} \tag{65}$$

For simplicity, τ is taken as independent of the frequency.

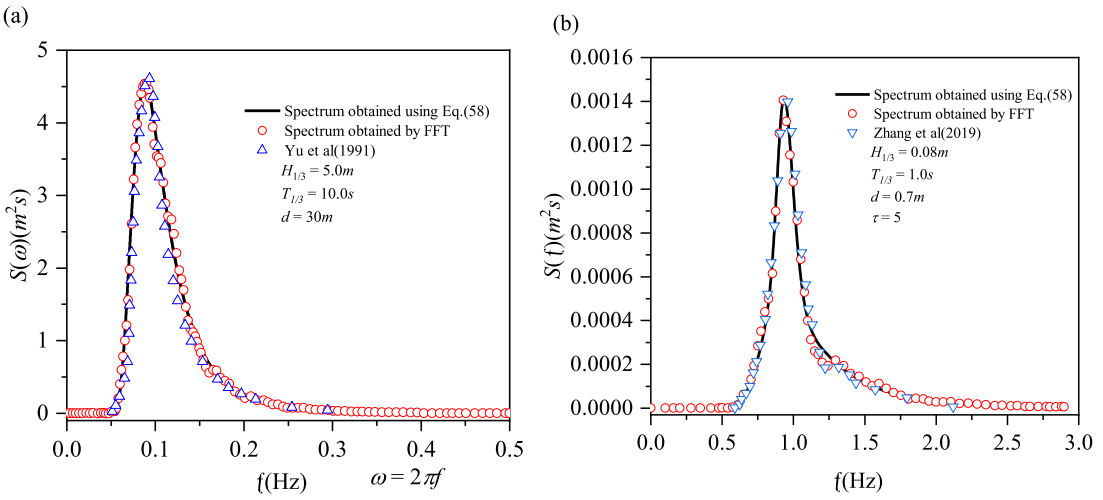

Fig. 12. Comparisons between the frequency spectra.

The complex amplitude $\xi_s^{(j)}/A$ of the jth-cylinder's displacement in the direction of the sth DOF for unit incident wave amplitude has been obtained in Section 2. Some examples for $\left|\xi_s^{(j)}/A\right|$ are shown in Figs. 6 and 7 of sub-Section 3.2. Considering that the object studied in this paper is a linear system, the time series of the displacements of the jth-cylinder in the sth-direction in the presence of multidirectional irregular waves can be expressed as

$$\Xi_s^{(j)}(t) = \mathrm{Re}\left\{\sum_{\mu=1}^{M}\sum_{\nu=1}^{N}\left|T_s^{(j)}(\overline{\omega}_\mu,\theta_\nu)\right| a_{\mu\nu}\mathrm{e}^{-\mathrm{i}\left[\omega_{\mu\nu}t-\varepsilon_{\mu\nu}-\alpha_{\mu\nu}\right]}\right\} \tag{66}$$

where $T_s^{(j)}(\overline{\omega}_\mu,\theta_\nu)$ is $\xi_s^{(j)}/A$ when the angular frequency of incident waves is $\overline{\omega}_\mu$, and the incidence angle is θ_ν. $\alpha_{\mu\nu} = \arctan\frac{\mathrm{Im}\left[T_s^{(j)}(\overline{\omega}_\mu,\theta_\nu)\right]}{\mathrm{Re}\left[T_s^{(j)}(\overline{\omega}_\mu,\theta_\nu)\right]}$.

Subsequently, the time series of the multidirectional irregular waves are obtained using Eq. (50). In the calculation, $M = 300$ and $N = 100$ are used. For verification, we carried out a fast Fourier transform (FFT) analysis on the obtained irregular waves time series to obtain the frequency spectrum and compare it with the frequency spectrum calculated with Eq. (58). The two examples (Yu et al., 1991; Zhang et al., 2019) of comparison are shown in Fig. 12, both of which are in good agreement.

With Eq. (66), the time series of the displacements of the jth-cylinder in the sth-direction in the presence of multidirectional irregular incident waves can be obtained. Then, the frequency spectrum can be obtained by FFT analysis of the time series. Next, the motions of an array of four truncated cylinders in the presence of the multidirectional irregular incident waves are calculated. As shown in Fig. 5, each cylinder has a radius of a, a draught of $h = 0.5a$. The spacing L and water depths are $4a$ and $10a$, respectively. The significant wave height $H_{1/3} = 5.0$ m, significant period $T_{1/3} = 10.0$ s, and principal wave direction $\theta_0 = 0^\circ$. The surge time series ($\Xi_1^{(1)}(t)$) of cylinder 1 for different directional spreading parameter τ are shown in Fig. 13. The time series of other DOFs and other cylinders are similar.

By performing FFT analysis on the surge time series in Fig. 13, the frequency spectra of the surge of cylinder 1 for different directional spreading parameters τ can be obtained. Similarly, the frequency spectra of other motion modes can also be obtained. The frequency spectra of each DOF for cylinders 1 and 4 are shown in Fig. 14 as representatives. As shown in Fig. 14, the larger the τ, the higher the spectral peaks of the cylinder's surge and pitch. This result is because the larger the directional spreading parameter τ, the narrower the directional distribution is. Therefore, the incident wave energy is more concentrated in the principal direction (i.e. the surge direction for the case investigated), resulting in greater surge and pitch responses. When τ becomes smaller, the incident wave energy is distributed in a wider direction, resulting in higher spectral peaks of sway and roll in this example.

6. Conclusion

In this paper, the hydrodynamic responses of a truncated-cylinder array in the presence of incident waves are studied. Relative motions are allowed among the cylinders in the array, with each cylinder allowed to oscillate with five DOFs: surge, sway, heave, roll, and pitch. A semi-analytical method is developed to deal with the hydrodynamic problem of interactions among waves and the array with relative motions consisting of truncated cylinders, in which the radiation–diffraction velocity potential induced by the array motion is expressed by the linear combination of the oscillation

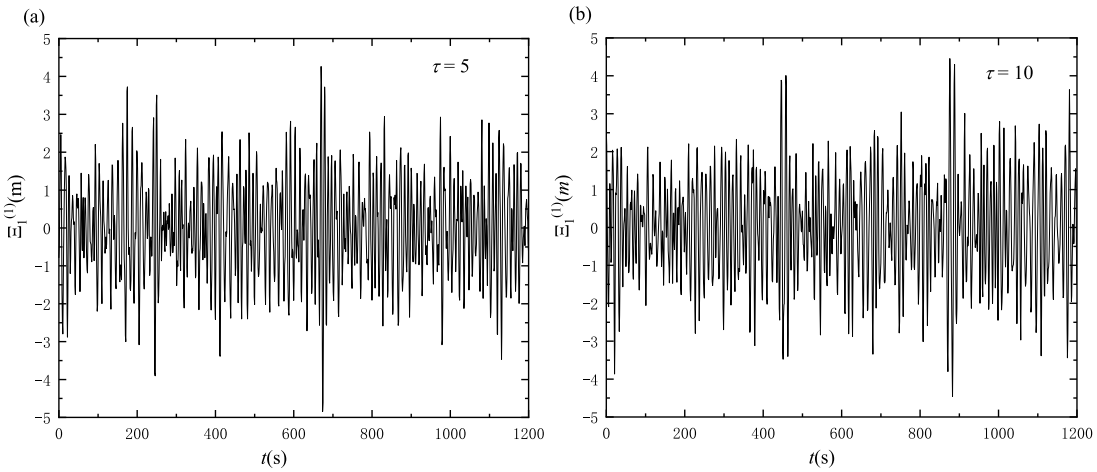

Fig. 13. Surge time series of cylinder 1 for different directional spreading parameter τ ($H_{1/3} = 5.0$ m, $T_{1/3} = 10.0$ s).

amplitudes to be solved in each direction of each cylinder, and then the radiation–diffraction hydrodynamic forces expressed by the oscillation amplitudes to be solved is obtained. Considering the balance among wave excitation forces, radiation–diffraction hydrodynamic forces, inertia forces of cylinder array, restoring forces, and other damping forces (damping forces other than radiation damping forces), the amplitude in each DOF of each cylinder and the radiation and diffraction velocity potentials of the array are obtained.

Subsequently, the amplitudes of every DOF of the array in the presence of incident waves are computed. Variations in the amplitude of each DOF of the cylinder in the array with dimensionless wavenumbers for cases with different incidence angles and cylinder spacings are obtained, and the amplitude distributions of free surface elevation for different wavenumbers are given. Furthermore, extensions to the situation in the presence of the multidirectional irregular waves are presented, and time series and frequency spectra of oscillation responses of cylinders are given.

Finally, the WEC array is analyzed based on 1-DOF model and 5-DOF models to investigate the influence of the multi-DOF model on hydrodynamic responses and wave energy extraction performances (capture width and interaction factor). Notably, the results obtained using the 5-DOF model differ greatly from those of the 1-DOF model in terms of oscillation amplitudes and wave energy extraction performances. It is suggested that the 5-DOF model should be used to analyze such cylinder arrays, especially in studying their wave extraction performances.

CRediT authorship contribution statement

Xiaohui Zeng: Conceptualization, Methodology, Supervision, Writing – original draft, Writing – review & editing. **Qi Wang:** Conceptualization, Methodology, Software, Data curation, Writing – original draft, Writing – review & editing. **Min Shi:** Data curation, Validation, Writing – review & editing. **Yuanshun Kang:** Conceptualization, Methodology, Software, Data curation, Writing – original draft, Writing – review & editing. **Fajun Yu:** Validation, Writing – review & editing.

Declaration of competing interest

The authors declare that they have no known competing financial interests or personal relationships that could have appeared to influence the work reported in this paper.

Data availability

Data will be made available on request.

Acknowledgments

This work was supported by the National Natural Science Foundation of China (grant no. 11672306), the Strategic Priority Research Program of the Chinese Academy of Sciences (grant no. XDB22020101), the open fund of the State Key Laboratory of coastal and offshore engineering, China, Dalian University of Technology, China (grant no. LP21V1), the young scientist cultivation fund of Harbin Engineering University, China (grant no. 79000001).

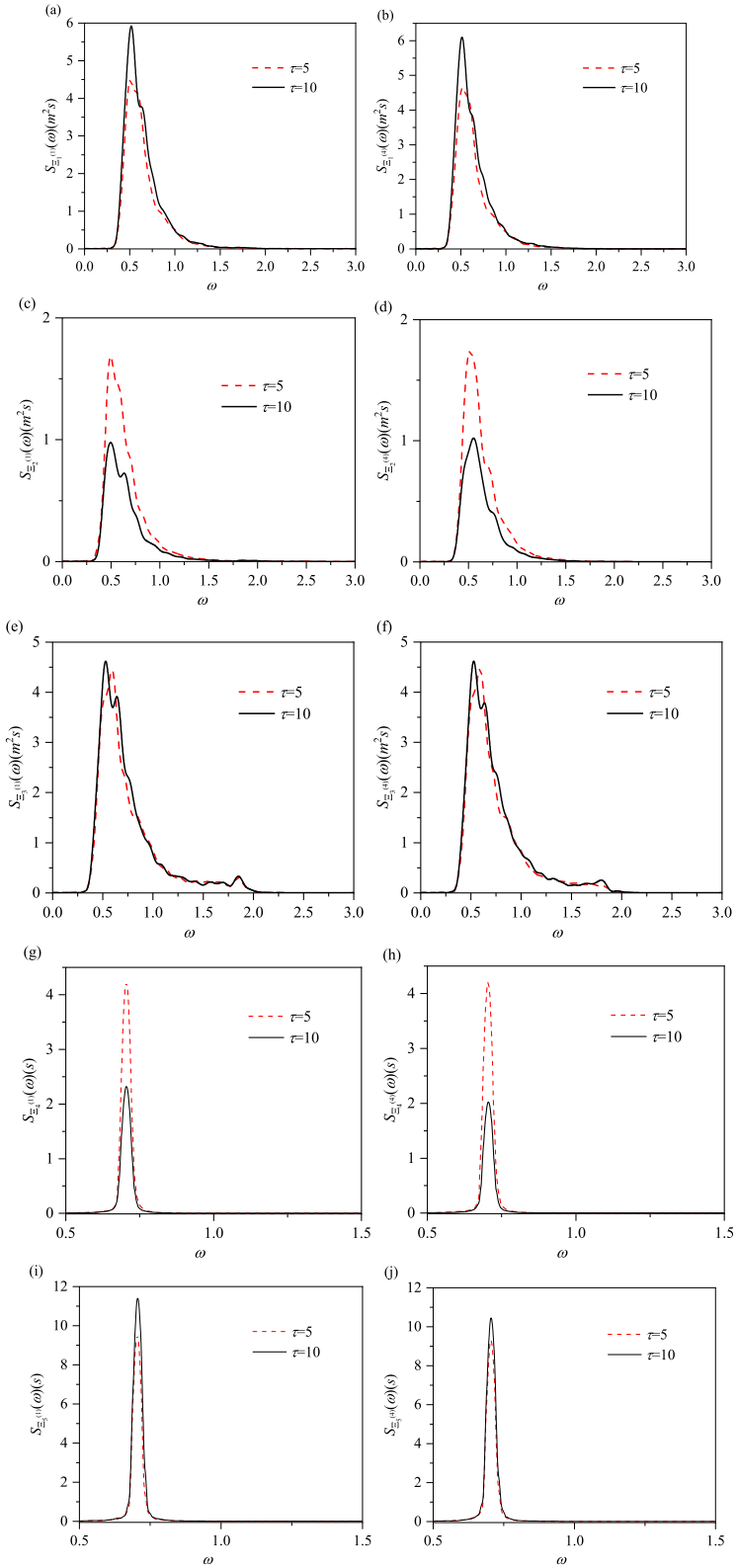

Fig. 14. Frequency spectra of each degree of freedom of cylinder 1 (a, c, e, g, i) and cylinder 4 (b, d, f, h, j) for different τ ($H_{1/3} = 5.0$ m, $T_{1/3} = 10.0$ s).

Appendix A. Diffraction solution

The amplitude of the ambient incident wave is A, the angular frequency is ω_0. The incidence angle of the ambient wave is at an angle of β with the positive direction of X-axis. Then the velocity potential of the ambient incident wave in the local cylindrical coordinate $o_j r_j \theta_j z_j$ at cylinder j is (Newman, 1977):

$$\varphi_I = -\frac{\mathrm{i}gA}{\omega_0} \sum_{m=-\infty}^{\infty} I_j \mathrm{e}^{\mathrm{i}m(\pi/2-\beta)} \cdot Z_0(z) J_m\left(k_0 r_j\right) \mathrm{e}^{\mathrm{i}m\theta_j}, \tag{A.1}$$

where g denotes the gravitational acceleration, $I_j = \mathrm{e}^{\mathrm{i}k_0(X_j \cos\beta + Y_j \sin\beta)}$ the phase factor, (X_j, Y_j) the coordinate of the axis of cylinder j in the global coordinate system, $Z_0 = \cosh k_0(z+d)/\cosh k_0 d$, J_m the mth-order Bessel function of the first kind, and wavenumber k_0 satisfies the dispersion relationship $k_0 \tanh k_0 d = \omega_0^2/g$.

In the coordinate system $o_i r_i \theta_i z_i$, the velocity potential of the diffracted waves in the exterior region of cylinder i is:

$$\varphi_{D0-E}^{(i)} = -\frac{\mathrm{i}gA}{\omega_0} \sum_{m=-\infty}^{\infty} \left[A_{0m}^{(i)} Z_0(z) H_m(k_0 r_i) + \sum_{n=1}^{\infty} A_{nm}^{(i)} Z_n(z) K_m(k_n r_i) \right] \mathrm{e}^{\mathrm{i}m\theta_i}, \tag{A.2}$$

where $A_{nm}^{(i)}$ is the undetermined complex coefficients, H_m the mth-order Hankel function of the first kind and K_m the mth-order modified Bessel function of the second kind. $Z_n = \cos k_n(z+d)$ is the characteristic function in z direction for $n \geq 1$ and wave number k_n is given by positive real roots of $k_n \tan k_n d = -\omega_0^2/g$.

Eqs. (A.1) and (A.2) can be written in matrix form:

$$\varphi_I = -\frac{\mathrm{i}gA}{\omega} \cdot \mathbf{a_j}^T \boldsymbol{\psi}_\mathbf{j}^\mathbf{I}, \tag{A.3}$$

$$\varphi_{D0-E}^{(i)} = -\frac{\mathrm{i}gA}{\omega_0} \cdot \mathbf{A_i}^T \boldsymbol{\psi}_\mathbf{i}^{\mathbf{D-E}}, \tag{A.4}$$

where the superscript T indicates the transpose. Elements of each vector are

$$\begin{aligned} \mathbf{a_j}(n, m) &= \begin{cases} I_j \mathrm{e}^{\mathrm{i}m(\pi/2-\beta)}, & n = 0, \\ 0, & n \geq 1, \end{cases} \\ \boldsymbol{\psi}_\mathbf{j}^\mathbf{I}(n, m) &= \begin{cases} Z_0(z) J_m\left(k_0 r_j\right) \mathrm{e}^{\mathrm{i}m\theta_j}, & n = 0, \\ Z_n(z) I_m\left(k_n r_j\right) \mathrm{e}^{\mathrm{i}m\theta_j}, & n \geq 1, \end{cases} \end{aligned} \tag{A.5}$$

$$\boldsymbol{\psi}_\mathbf{i}^{\mathbf{D-E}}(n, m) = \begin{cases} Z_0(z) H_m(k_0 r_i) \mathrm{e}^{\mathrm{i}m\theta_i}, & n = 0, \\ Z_n(z) K_m(k_n r_i) \mathrm{e}^{\mathrm{i}m\theta_i}, & n \geq 1, \end{cases} \tag{A.6}$$

$\boldsymbol{\psi}_\mathbf{i}^{\mathbf{D-E}}$ can be rewritten in term of the representation of it in the coordinate system $o_j r_j \theta_j z_j$ by using Graf's addition theorems for Bessel functions:

$$\boldsymbol{\psi}_\mathbf{i}^{\mathbf{D-E}}(n, m) = \begin{cases} \displaystyle\sum_{l=-\infty}^{\infty} H_{m-l}\left(k_0 R_{ij}\right) \mathrm{e}^{\mathrm{i}\alpha_{ij}(m-l)} \cdot Z_0(z) J_l\left(k_0 r_j\right) \mathrm{e}^{\mathrm{i}l\theta_j}, & n = 0, \\ \displaystyle\sum_{l=-\infty}^{\infty} K_{m-l}\left(k_n R_{ij}\right) \mathrm{e}^{\mathrm{i}\alpha_{ij}(m-l)} (-1)^l \cdot Z_n(z) I_l\left(k_n r_j\right) \mathrm{e}^{\mathrm{i}l\theta_j}, & n \geq 1, \end{cases} \tag{A.7}$$

where R_{ij} is the distance between the origins o_i and o_j, α_{ij} the azimuthal angle of o_j relative to o_i (shown in Fig. 1(c)).

And it can be further written in the matrix form:

$$\boldsymbol{\psi}_\mathbf{i}^{\mathbf{D-E}} = \mathbf{T_{ij}} \boldsymbol{\psi}_\mathbf{j}^\mathbf{I}, \tag{A.8}$$

where $\mathbf{T_{ij}}$ is a matrix representing the coordinate transformation from i to j:

$$\mathbf{T_{ij}}(n, m, l) = \begin{cases} H_{m-l}\left(k_0 R_{ij}\right) \mathrm{e}^{\mathrm{i}\alpha_{ij}(m-l)}, & n = 0, \\ K_{m-l}\left(k_n R_{ij}\right) \mathrm{e}^{\mathrm{i}\alpha_{ij}(m-l)} (-1)^l, & n \geq 1. \end{cases} \tag{A.9}$$

Therefore, the diffraction potential in the exterior region of cylinder i represented by Eq. (A.4) can be written as follows in the coordinate system $o_j r_j \theta_j z_j$:

$$\varphi_{D0-E}^{(i)}|_j = -\frac{\mathrm{i}gA}{\omega_0} \mathbf{A_i}^T \mathbf{T_{ij}} \boldsymbol{\psi}_\mathbf{j}^\mathbf{I}. \tag{A.10}$$

The total incident waves of cylinder j consist of the ambient incident wave and the diffracted waves from other cylinders:

$$\varphi_I^{(j)} = \varphi_I + \sum_{i=1,i\neq j}^{N} \varphi_{D0-E}^{(i)}|_j = -\frac{igA}{\omega_0}\left(\mathbf{a_j}^T + \sum_{i=1,i\neq j}^{N} \mathbf{A_i}^T \mathbf{T_{ij}}\right)\boldsymbol{\psi}_\mathbf{j}^\mathbf{I}. \tag{A.11}$$

The total incident waves and total diffracted waves in the vicinity of cylinder j can be related by its isolated-body inherent diffraction transfer matrix $\mathbf{B_j^E}$ (Kagemoto and Yue, 1986):

$$\mathbf{A_j} = \mathbf{B_j^E}\left(\mathbf{a_j} + \sum_{i=1,i\neq j}^{N} \mathbf{T_{ij}}^T \mathbf{A_i}\right), \quad j = 1, 2, \ldots, N, \tag{A.12}$$

Following the method given in Kagemoto and Yue (1986), elements of diffraction transfer matrix $\mathbf{B_j^E}$ and $\mathbf{B_j^C}$ for an isolated truncated circular cylinder are obtained, which are listed as follows:

$$\mathbf{B_j^E}(0,0,m) = -\frac{J_m'(k_0a_j)}{H_m'(k_0a_j)} + \frac{D_{mq}^n \cosh k_0 d}{H_m'(k_0a_j)N_0^{1/2}e^{\mathrm{i}m(\pi/2-\beta)}}, \quad n=0, q=0, \tag{A.13}$$

$$\mathbf{B_j^E}(q,0,m) = \frac{D_{mq}^n}{K_m'(k_qa_j)N_q^{1/2}e^{\mathrm{i}m(\pi/2-\beta)}}, \quad n=0, q\geq 1, \tag{A.14}$$

$$\mathbf{B_j^E}(0,n,m) = \frac{D_{m0}^n \cosh k_0 d}{H_m'(k_0a_j)N_0^{1/2}}, \quad n\geq 1, q=0, \tag{A.15}$$

$$\mathbf{B_j^E}(q,n,m) = \begin{cases} \frac{D_{mq}^n}{K_m'(k_qa_j)N_q^{1/2}}, & n\geq 1, q\geq 1, q\neq n, \\ -\frac{I_m'(k_qa_j)}{K_m'(k_qa_j)} + \frac{D_{mq}^n}{K_m'(k_qa_j)N_q^{1/2}}, & n\geq 1, q\geq 1, q=n, \end{cases} \tag{A.16}$$

$$\mathbf{B_j^C}(0,0,m) = \frac{C_{m0}^n}{2a_j^{|m|}\mathrm{i}^m}, \quad n=0, p=0, \tag{A.17}$$

$$\mathbf{B_j^C}(p,0,m) = \frac{C_{mp}^n}{I_m\left(p\pi a_j/(d-h_j)\right)\mathrm{i}^m}\cos\left(\frac{p\pi(z+d)}{d-h_j}\right), \quad n=0, p\geq 1, \tag{A.18}$$

$$\mathbf{B_j^C}(0,n,m) = \frac{C_{m0}^n}{2a_j^{|m|}}, \quad n\geq 1, p=0, \tag{A.19}$$

$$\mathbf{B_j^C}(p,n,m) = \frac{C_{mp}^n}{\mathrm{I}_m\left(p\pi a_j/(d-h_j)\right)}\cos\left(\frac{p\pi(z+d)}{d-h_j}\right), \quad n\geq 1, p\geq 1, \tag{A.20}$$

where C_{mp}^n and D_{mq}^n are the unknown coefficients of the velocity potential of an isolated truncated cylinder in the core region and exterior region respectively, Following the method given in Garrett (1971), they are obtained by solving

$$\begin{cases} C_{mp}^n + \sum_{q=0}^{\infty} F_{mpq} D_{mq}^n = R_{mp}^n \\ D_{mq}^n - \sum_{p=0}^{\infty} G_{mqp} C_{mp}^n = 0 \end{cases}, \tag{A.21}$$

where

$$F_{mpq} = \begin{cases} -\frac{2H_m(k_0a_j)k_0(d-h_j)(-1)^p \sinh k_0(d-h_j)}{H_m'(k_0a_j)\cdot N_0^{1/2}\cdot\left[k_0{}^2(d-h_j)^2+p^2\pi^2\right]}, & q=0, \\ -\frac{2K_m(k_qa_j)k_q(d-h_j)(-1)^p \sin k_q(d-h_j)}{K_m'(k_qa_j)\cdot N_q^{1/2}\cdot\left[k_q{}^2(d-h_j)^2-p^2\pi^2\right]}, & q\geq 1, \end{cases} \tag{A.22}$$

$$G_{mqp} = \begin{cases} \frac{|m|\cdot\sin k_q(d-h_j)}{2a_j\cdot d\cdot k_q{}^2 N_q^{1/2}}, & p=0, \\ \frac{I_m'(\frac{p\pi a_j}{d-h_j})\cdot p\pi(d-h)(-1)^p\cdot\sin k_q(d-h_j)}{I_m(\frac{p\pi a_j}{d-h_j})\cdot d\cdot N_q^{1/2}\cdot[k_q{}^2(d-h_j)^2-p^2\pi^2]}, & p\geq 1, \end{cases} \tag{A.23}$$

$$R_{mp}^n = \begin{cases} 2\mathrm{i}^m[J_m(k_0a_j) - \frac{J_m'(k_0a_j)}{H_m'(k_0a_j)}H_m(k_0a_j)]\cdot\frac{(-1)^p\cdot k_0(d-h_j)\sinh k_0(d-h_j)}{\cosh k_0 d\cdot[k_0{}^2(d-h_j)^2+p^2\pi^2]}, & n=0, \\ 2[I_m(k_na_j) - \frac{I_m'(k_na_j)}{K_m'(k_na_j)}K_m(k_na_j)]\cdot\frac{(-1)^p k_n(d-h_j)\sin k_n(d-h_j)}{k_n{}^2(d-h_j)^2-p^2\pi^2}, & n\geq 1. \end{cases} \tag{A.24}$$

By combining the equations of all $\mathbf{A_j}$ as shown in Eq. (A.12), we can get

$$\begin{aligned}
&\begin{bmatrix} \mathbf{A_1} \\ \mathbf{A_2} \\ \vdots \\ \mathbf{A_N} \end{bmatrix} = \begin{bmatrix} \mathbf{B_1^E} & 0 & \cdots & 0 \\ 0 & \mathbf{B_2^E} & \cdots & 0 \\ \vdots & \vdots & \ddots & \vdots \\ 0 & 0 & \cdots & \mathbf{B_N^E} \end{bmatrix} \cdot \left\{ \begin{bmatrix} \mathbf{a_1} \\ \mathbf{a_2} \\ \vdots \\ \mathbf{a_N} \end{bmatrix} + \begin{bmatrix} 0 & \mathbf{T_{21}^T} & \cdots & \mathbf{T_{N1}^T} \\ \mathbf{T_{12}^T} & 0 & \cdots & \mathbf{T_{N2}^T} \\ \vdots & \vdots & \ddots & \vdots \\ \mathbf{T_{1N}^T} & \mathbf{T_{2N}^T} & \vdots & 0 \end{bmatrix} \cdot \begin{bmatrix} \mathbf{A_1} \\ \mathbf{A_2} \\ \vdots \\ \mathbf{A_N} \end{bmatrix} \right\} \\
&\Rightarrow \begin{bmatrix} \mathbf{A_1} \\ \mathbf{A_2} \\ \vdots \\ \mathbf{A_N} \end{bmatrix} = \left[\mathbf{E} - \begin{bmatrix} \mathbf{B_1^E} & 0 & \cdots & 0 \\ 0 & \mathbf{B_2^E} & \cdots & 0 \\ \vdots & \vdots & \ddots & \vdots \\ 0 & 0 & \cdots & \mathbf{B_N^E} \end{bmatrix} \cdot \begin{bmatrix} 0 & \mathbf{T_{21}^T} & \cdots & \mathbf{T_{N1}^T} \\ \mathbf{T_{12}^T} & 0 & \cdots & \mathbf{T_{N2}^T} \\ \vdots & \vdots & \ddots & \vdots \\ \mathbf{T_{1N}^T} & \mathbf{T_{2N}^T} & \vdots & 0 \end{bmatrix} \right]^{-1} \cdot \begin{bmatrix} \mathbf{B_1^E} & 0 & \cdots & 0 \\ 0 & \mathbf{B_2^E} & \cdots & 0 \\ \vdots & \vdots & \ddots & \vdots \\ 0 & 0 & \cdots & \mathbf{B_N^E} \end{bmatrix} \cdot \begin{bmatrix} \mathbf{a_1} \\ \mathbf{a_2} \\ \vdots \\ \mathbf{a_N} \end{bmatrix}
\end{aligned} \tag{A.25}$$

The unknown coefficient vector $\mathbf{A_j}$ can be obtained by solving this linear system with $N(n_0{+}1)(2m_0{+}1)$ unknowns. For further matrix construction of $\mathbf{B_j^E}$ and $\mathbf{T_{ij}}$, refer to Zeng et al. (2016).

The total velocity potential in the exterior region of cylinder j for the diffraction problem of a truncated-cylinder array can be written as follows:

$$\varphi_{ID-E}^{(j)} = -\frac{\mathrm{i}gA}{\omega_0} \left[\mathbf{A_j}^T \boldsymbol{\psi}_\mathbf{j}^{\mathbf{D-E}} + \left(\mathbf{a_j}^T + \sum_{i=1, i\neq j}^{N} \mathbf{A_i}^T \mathbf{T_{ij}} \right) \boldsymbol{\psi}_\mathbf{j}^{\mathbf{I}} \right]. \tag{A.26}$$

Similarly, the total velocity potential in the core region of cylinder j has the form:

$$\varphi_{ID-C}^{(j)} = -\frac{igA}{\omega_0} \left(\mathbf{a_j}^T + \sum_{i=1, i\neq j}^{N} \mathbf{A_i}^T \mathbf{T_{ij}} \right) \left(\mathbf{B_j^C} \right)^T \boldsymbol{\psi}_\mathbf{j}^{\mathbf{D-C}}, \tag{A.27}$$

where $\mathbf{B_j^C}$ are given in Appendix A. Elements of vector $\boldsymbol{\psi}_\mathbf{j}^{\mathbf{D-C}}$ are

$$\boldsymbol{\psi}_\mathbf{j}^{\mathbf{D-C}}(p, m) = \begin{cases} r_j^{|m|} \mathrm{e}^{\mathrm{i}m\theta_j}, & p = 0, \\ I_m \left(\frac{p\pi r_j}{d-h_j} \right) \mathrm{e}^{\mathrm{i}m\theta_j}, & p \geq 1. \end{cases} \tag{A.28}$$

Appendix B. Radiation solution of an isolated cylinder

Following the method give in Yeung (1981) and Sabuncu and Calisal (1981), $C_{R_{pm}}^s$ and $D_{R_{nm}}^s$ can be solved from equations:

$$\begin{cases} C_{R_{pm}}^s + \sum_{q=0}^{\infty} F_{mpq} D_{R_{qm}}^s = R_{R_{pm}}^s \\ D_{R_{qm}}^s - \sum_{p=0}^{\infty} G_{mqp} C_{R_{pm}}^s = S_{R_{qm}}^s \end{cases}. \tag{B.1}$$

In the above formula,

$$R_{R_{pm}}^s = -\frac{2}{d-h} \int_{-d}^{-h_j} \lambda_{ms} \Lambda_s(a_j, z) \cos\left[\frac{p\pi (z+d)}{d-h_j} \right] dz, \tag{B.2}$$

$$S_{R_{qm}}^s = \frac{\lambda_{ms}}{k_q d} \int_{-d}^{-h_j} \frac{\partial \Lambda_s(a_j, z)}{\partial r} Z_q(z)\, dz + \frac{\lambda_{ms}}{k_q d} \int_{-h_j}^{0} f_s(z) Z_q(z)\, dz, \tag{B.3}$$

where

$$f_s(z) = \begin{cases} 1, & s = 1, 2, \\ 0, & s = 3, \\ -(z - \overline{z}), & s = 4, \\ (z - \overline{z}), & s = 5, \end{cases} \tag{B.4}$$

$$\Lambda_s = \begin{cases} 0, & s = 1, 2, \\ \frac{1}{2(d-h_j)}\left[(z+d)^2 - \frac{r_j^2}{2}\right], & s = 3, \\ \frac{r_j}{2(d-h_j)}\left[(z+d)^2 - \frac{r_j^2}{4}\right], & s = 4, \\ -\frac{r_j}{2(d-h_j)}\left[(z+d)^2 - \frac{r_j^2}{4}\right], & s = 5, \end{cases} \tag{B.5}$$

$$\lambda_{ms} = \begin{cases} m = 1: \begin{cases} \lambda_{11} = \lambda_{15} = \frac{1}{2} \\ \lambda_{13} = 0 \\ \lambda_{12} = \lambda_{14} = \frac{1}{2i} \end{cases}, \quad m = 0: \begin{cases} \lambda_{01} = \lambda_{05} = 0 \\ \lambda_{03} = 1 \\ \lambda_{02} = \lambda_{04} = 0 \end{cases} \\ m = -1: \begin{cases} \lambda_{-11} = \lambda_{-15} = \frac{1}{2} \\ \lambda_{-13} = 0 \\ \lambda_{-12} = \lambda_{-14} = -\frac{1}{2i} \end{cases}, \quad m = others: \lambda_{ms} = 0 \end{cases} \tag{B.6}$$

References

Balitsky, P., Fernandez, G., Stratigaki, V., Troch, P., 2018. Assessment of the power output of a two-array clustered WEC farm using a BEM solver coupling and a Wave-Propagation Model. Energies 11 (11), 2907.

Bennetts, L.G., Peter, M.A., Montiel, F., 2017. Localisation of Rayleigh–Bloch waves and damping of resonant loads on arrays of vertical cylinders. J. Fluid Mech. 813, 508–527.

Chatjigeorgiou, I.K., 2019. Semi-analytical solution for the water wave diffraction by arrays of truncated circular cylinders in front of a vertical wall. Appl. Ocean Res. 88, 147–159.

Chatjigeorgiou, I.K., Chatziioannou, K., Mazarakos, T., 2019. Near trapped modes in long array of truncated circular cylinders. J. Waterw. Port Coast. Ocean Eng. 145 (1), 04018035.

Child, B.F.M., Venugopal, V., 2010. Optimal configurations of wave energy device arrays. Ocean Eng. 37 (16), 1402–1417.

Evans, D.V., Porter, R., 1997. Near-trapping of waves by circular arrays of vertical cylinders. Appl. Ocean Res. 19 (2), 83–99.

Falnes, J., 1980. Radiation impedance matrix and optimum power absorption for interacting oscillators in surface waves. Appl. Ocean Res. 2 (2), 75–80.

Falnes, J., 2002. Ocean Waves and Oscillating Systems, Linear Interactions Including Wave-Energy Extraction, first ed. Cambridge University Press, Cambridge.

Flavia, F.F., Meylan, M.H., 2019. An extension of general identities for 3D water-wave diffraction with application to the Diffraction Transfer Matrix. Appl. Ocean Res. 84, 279–290.

Garrett, C.J.R., 1971. Wave forces on a circular dock. J. Fluid Mech. 46 (1), 129–139.

Giassi, M., Engström, J., Isberg, J., Göteman, M., 2020. Comparison of wave energy park layouts by experimental and numerical methods. J. Mar. Sci. Eng. 8 (10), 750.

Goda, Y.A., 1999. A comparative review on the functional forms of directional wave spectrum. Coast. Eng. J. 41 (1), 1–20.

Göteman, M., 2017. Wave energy parks with point-absorbers of different dimensions. J. Fluids Struct. 74, 142–157.

Kagemoto, H., Yue, D., 1986. Interactions among multiple three-dimensional bodies in water waves: an exact algebraic method. J. Fluid Mech. 166, 189–209.

Kashiwagi, M., 2017. Hydrodynamic interactions of multiple bodies with water waves. Int. J. Offshore and Polar Eng. 27 (2), 113–122.

Konispoliatis, D.N., Mavrakos, S.A., 2016. Hydrodynamic analysis of an array of interacting free-floating oscillating water column (OWC's) devices. Ocean Eng. 111, 179–197.

Linton, C.M., Evans, D.V., 1990. The interaction of waves with arrays of vertical circular cylinders. J. Fluid Mech. 215, 549–569.

Longuet-Higgins, M.S., Cartwright, D.E., Smith, N.D., 1963. Observations of the directional spectrum of sea waves using the motions of floating buoy. In: Ocean Wave Spectra. Prentice-HallInc., Englewood Cliffs, N.J.USA, pp. 111–136.

Maniar, H.D., Newman, J.N., 1997. Wave diffraction by a long array of cylinders. J. Fluid Mech. 339, 309–330.

Matsui, T., Tamaki, T., 1981. Hydrodynamic interaction between groups of vertical axisymmetric bodies floating in waves, In: International symposium on hydrodynamics in ocean engineering, pp. 817–836.

Mavrakos, S.A., 1991. Hydrodynamic coefficients for groups of interacting vertical axisymmetric bodies. Ocean Eng. 18 (5), 485–515.

Mavrakos, S.A., Chatjigeorgiou, I.K., Konispoliatis, D.N., 2018. Wave diffraction on arrays of vertical truncated cylindrical bodies. In: ASME 2018 37th International Conference on Ocean, Offshore and Arctic Engineering. vol. 9, Offshore Geotechnics.

Mavrakos, S.A., Koumoutsakos, P., 1987. Hydrodynamic interaction among vertical axisymmetric bodies restrained in waves. Appl. Ocean Res. 9 (3), 128–140.

McGuinness, J.P., Thomas, G., 2016. Hydrodynamic optimisation of small arrays of heaving point absorbers. J. Ocean Eng. Mar. Energy 2 (4), 439–457.

Mcnatt, J.C., Venugopal, V., Forehand, D., 2015. A novel method for deriving the diffraction transfer matrix and its application to multi-body interactions in water waves. Ocean Eng. 94 (jan.15), 173–185.

Newman, J.N., 1977. Marine Hydrodynamics. MIT Press, Cambridge.

Odijie, A.C., Wang, F., Ye, J., 2017. A review of floating semisubmersible hull systems: Column stabilized unit. Ocean Eng. 144, 191–202.

Okhusu, M., 1974. Hydrodynamic forces on multiple cylinders in waves. In: Int. Symposium on the Dynamics of Marine Vehicles and Structures in Waves. Paper 12, University College London, London, pp. 107–112.

Penalba, M., Touzón, I., Lopez-Mendia, J., Nava, V., 2017. A numerical study on the hydrodynamic impact of device slenderness and array size in wave energy farms in realistic wave climates. Ocean Eng. 142, 224–232.

Sabuncu, T., Calisal, S., 1981. Hydrodynamic coefficients for vertical circular cylinders at finite depth. Ocean Eng. 8 (1), 25–63.

Sharp, C., DuPont, B., 2018. Wave energy converter array optimization: A genetic algorithm approach and minimum separation distance study. Ocean Eng. 163, 148–156.

Siddorn, P., Taylor, R.Eatock., 2008. Diffraction and independent radiation by an array of floating cylinders. Ocean Eng. 35 (13), 1289–1303.

Simon, M.J., 1982. Multiple scattering in arrays of axisymmetric wave-energy devices. Part 1. A matrix method using a plane-wave approximation. J. Fluid Mech. 120, 1–25.

Singh, J., Babarit, A., 2014. A fast approach coupling Boundary Element Method and plane wave approximation for wave interaction analysis in sparse arrays of wave energy converters. Ocean Eng. 85, 12–20.
Spring, B.H., Monkmeyer, P.L., 1975. Interaction of plane waves with vertical cylinders. Coast. Eng. 1974, 1828–1847.
Thomas, G.P., Evans, D.V., 1981. Arrays of three-dimensional wave-energy absorbers. J. Fluid Mech. 108, 67–88.
Tokić, G., Yue, D.K., 2019. Hydrodynamics of periodic wave energy converter arrays. J. Fluid Mech. 862, 34–74.
Wang, J.F., Li, J.D., Weng, N.M., 2004. Coupled motions of two ships in irregular waves in time domain. J. Mar. Sci. Appl. 3 (2), 1–6.
Williams, A.N., Abul-Azm, A.G., 1989. Hydrodynamic interactions in floating cylinder arrays—II. Wave radiation. Ocean Eng. 16 (3), 217–263.
Yeung, R.W., 1981. Added mass and damping of a vertical cylinder in finite-depth waters. Appl. Ocean Res. 3 (3), 119–133.
Yilmaz, O., 1998. Hydrodynamic interactions of waves with group of truncated vertical cylinders. J. Waterway Port Coastal and Ocean Eng. 124 (5), 272–279.
Yu, Y., Liu, S., Li, L., 1991. Numerical simulation of multi-directional random seas, In: The First International Offshore and Polar Engineering Conference. III: pp. 26-32.
Zeng, X.H., Shi, M., Huang, S., 2016. Hydrodynamic interactions of water waves with a group of independently oscillating truncated circular cylinders. Acta Mech. Sinica 32 (5), 773–791.
Zeng, X.H., Tang, S.Y., 2013. The hydrodynamic interactions of an array of truncated circular cylinders as each cylinder oscillates independently with different prescribed modes. J. Hydrodyn. 25 (1), 27–38.
Zeng, X., Yu, F., Shi, M., Wang, Q., 2019. Fluctuation of magnitude of wave loads for a long array of bottom-mounted cylinders. J. Fluid Mech. 868, 244–285.
Zhang, Z., He, G., Wang, W., Liu, S., Wang, Z., 2020. Reduction of wave drift force on a truncated cylinder in a wide frequency band using the defect effects on cloaking phenomenon. Ocean Eng. 203, 107241.
Zhang, H., Liu, S., Li, J., Zhang, R., Hao, J., 2019. Interactions between multi-directional irregular waves and a pile group in a side-by-side arrangement: Statistical analysis. Coast. Eng. 147, 115–134.
Zhang, X., Song, X., Qiu, W., Yuan, Z., You, Y., Deng, N., 2018. Multi-objective optimization of Tension Leg Platform using evolutionary algorithm based on surrogate model. Ocean Eng. 148, 612–631.
Zhong, Q., Yeung, R.W., 2019. Wave-body interactions among energy absorbers in a wave farm. Appl. Energy 233, 1051–1064.